The Astrophysical Journal, 975:239 (21pp), 2024 November 10 https://doi.org/10.3847/1538-4357/ad7c42

The SDSS-V Black Hole Mapper Reverberation Mapping Project: A Kinematically Variable Broad-line Region and Consequences for the Masses of Luminous Quasars

Logan B. Fries[1], Jonathan R. Trump[1], Keith Horne[2], Megan C. Davis[1], Catherine J. Grier[3], Yue Shen[4,5], Scott F. Anderson[6], Tom Dwelly[7], Y. Homayouni[8,9], Sean Morrison[4], Jessie C. Runnoe[10], Benny Trakhtenbrot[11], Roberto J. Assef[12], Dmitry Bizyaev[13,14], W. N. Brandt[8,9,15], Peter Breiding[16], Joel Brownstein[17], Priyanka Chakraborty[18], P. B. Hall[19], Anton M. Koekemoer[20], Héctor J. Ibarra-Medel[21], Mary Loli Martínez-Aldama[22], C. Alenka Negrete[23], Kaike Pan[13], Claudio Ricci[24,25], Donald P. Schneider[8,9], Hugh W. Sharp[1], Theodore B. Smith[1], Zachary Stone[4], and Matthew J. Temple[24]

[1] Department of Physics, 196A Auditorium Road, Unit 3046, University of Connecticut, Storrs, CT 06269, USA; logan.fries@uconn.edu
[2] SUPA Physics and Astronomy, University of St. Andrews, St. Andrews, Fife KY16 9SS, UK
[3] Department of Astronomy, University of Wisconsin-Madison, Madison, WI 53706, USA
[4] Department of Astronomy, University of Illinois at Urbana-Champaign, Urbana, IL 61801, USA
[5] National Center for Supercomputing Applications, University of Illinois at Urbana-Champaign, Urbana, IL 61801, USA
[6] Astronomy Department, University of Washington, Box 351580, Seattle, WA 98195, USA
[7] Max-Planck-Institut für extraterrestrische Physik, Giessenbachstraße, 85748 Garching, Germany
[8] Department of Astronomy & Astrophysics, 525 Davey Lab, The Pennsylvania State University, University Park, PA 16802, USA
[9] Institute for Gravitation and the Cosmos, The Pennsylvania State University, University Park, PA 16802, USA
[10] Department of Physics and Astronomy, Vanderbilt University, Nashville, TN 37235, USA
[11] School of Physics and Astronomy, Tel Aviv University, Tel Aviv 69978, Israel
[12] Instituto de Estudios Astrofísicos, Facultad de Ingenieraía y Ciencias, Universidad Diego Portales, Av. Ejército Libertador 441, Santiago 8370191, Chile
[13] Apache Point Observatory and New Mexico State University, P.O. Box 59, Sunspot, NM 88349-0059, USA
[14] Sternberg Astronomical Institute, Moscow State University, Moscow, Russia
[15] Department of Physics, 104 Davey Lab, The Pennsylvania State University, University Park, PA 16802, USA
[16] The William H. Miller III Department of Physics & Astronomy, Johns Hopkins University, Baltimore, MD 21218, USA
[17] Department of Physics and Astronomy, University of Utah, 115 S. 1400 E., Salt Lake City, UT 84112, USA
[18] Center for Astrophysics—Harvard & Smithsonian, Cambridge, MA 02138, USA
[19] Department of Physics and Astronomy, York University, Toronto, ON M3J 1P3, Canada
[20] Space Telescope Science Institute, 3700 San Martin Dr., Baltimore, MD 21218, USA
[21] Universidad Nacional Autónoma de México, Instituto de Astronomía, AP 70-264, CDMX 04510, Mexico
[22] Astronomy Department, Universidad de Concepción, Casilla 160-C, Concepción 4030000, Chile
[23] CONAHCyT Research Fellow, Universidad Nacional Autónoma de México, Instituto de Astronomía, AP 70-264, CDMX 04510, Mexico
[24] Instituto de Estudios Astrofísicos, Facultad de Ingeniería y Ciencias, Universidad Diego Portales, Av. Ejército Libertador 441, Santiago, Chile
[25] Kavli Institute for Astronomy and Astrophysics, Peking University, Beijing 100871, People's Republic of China

Received 2024 July 13; revised 2024 September 16; accepted 2024 September 16; published 2024 November 6

Abstract

We present a velocity-resolved reverberation mapping analysis of the hypervariable quasar RM160 (SDSS J141041.25+531849.0) at $z = 0.359$ with 153 spectroscopic epochs of data representing a 10 yr baseline (2013–2023). We split the baseline into two regimes based on the 3× flux increase in the light curve: a "low state" phase during the years 2013–2019 and a "high state" phase during the years 2022–2023. The velocity-resolved lag profiles (VRLPs) indicate that gas with different kinematics dominates the line emission in different states. The Hβ VRLP begins with a signature of inflow onto the broad-line region (BLR) in the low state, while in the high state it is flatter with less signature of inflow. The Hα VRLP begins consistent with a virialized BLR in the low state, while in the high state shows a signature of inflow. The differences in the kinematics between the Balmer lines and between the low state and the high state suggests complex BLR dynamics. We find that the BLR radius and velocity (both FWHM and σ) do not obey a constant virial product throughout the monitoring period. We find that the BLR lags and continuum luminosity are correlated, consistent with rapid response of the BLR gas to the illuminating continuum. The BLR kinematic profile changes in unpredictable ways that are not related to continuum changes and reverberation lag. Our observations indicate that nonvirial kinematics can significantly contribute to observed line profiles, suggesting caution for black hole mass estimation in luminous and highly varying quasars like RM160.

Unified Astronomy Thesaurus concepts: Active galactic nuclei (16); Active galaxies (17); Quasars (1319); Supermassive black holes (1663)

1. Introduction

The optical spectra of active galactic nuclei (AGN) are characterized by a blue continuum and broad emission lines (e.g., C. K. Seyfert 1943). Broad emission lines are created when the continuum flux photoionizes a distribution of gas called the broad-line region (BLR). Since the BLR is located close to the central engine (black hole + accretion disk) and is assumed to be moving under orbits dominated by gravity (i.e., virialized; B. M. Peterson et al. 2004; M. C. Bentz et al. 2009; C. J. Grier et al. 2013), the emission lines are Doppler broadened by the high-velocity gas.

In L. B. Fries et al. (2023), we presented an analysis of dramatic variability of three broad emission lines (Mg II, Hβ, and Hα) in the quasar SDSS J141041.25+531849.0 (hereafter RM160). This quasar was observed to have normal "line breathing" behavior (i.e., the broad emission-line widths decrease with an increase in continuum flux and vice versa), but also exhibited dramatic broad emission-line radial-velocity variations, ranging from $\Delta v \sim 800$ to ~ 1600 km s^{-1}, relative to the systemic redshift. The radial-velocity variations are consistent with a multifaceted explanation: (1) a bulk inflow of the BLR gas with a gradient of higher velocity at smaller radii, (2) an azimuthal asymmetry circulating around in the inner regions of the BLR, and (3) stochastic flux-driven changes to the optimal emission region (i.e., line breathing; A. J. Barth et al. 2015; S. Wang et al. 2020). We presented this phenomenological model with the aim of further investigating the structure and kinematics of the BLR with reverberation mapping (R. D. Blandford & C. F. McKee 1982; B. M. Peterson 1993; E. M. Cackett et al. 2021).

Since the BLR is on the order of tens to hundreds of light-days in size, there are only a handful of studies that have resolved the BLR spatially using interferometric techniques (e.g., Gravity Collaboration et al. 2020), but these are only possible for low-redshift AGN. Since we cannot spatially resolve the BLR in most quasars, we must turn to other techniques. Reverberation mapping is a technique that trades spatial resolution for temporal resolution. The basic idea of reverberation mapping is that the flux variations in the broad emission lines closely follow (i.e., lag) the stochastic flux variations from the central engine. The lag (τ) between these two signals corresponds to the light-travel time for ionizing radiation emitted by the central engine to reach the BLR. The lag between the central engine and an arbitrary emission line corresponds to the "response-weighted radius" (or "optimal emission radius") of the given emission line using $R_{\rm BLR} = c\tau$. Probing different emission lines via reverberation mapping allows one to infer the structure of the BLR by understanding where different emission lines are most "optimally" emitted. Indeed, it has been found that higher-ionization lines respond to continuum variations more rapidly, indicating that the BLR is radially stratified (C. M. Gaskell & L. S. Sparke 1986; B. M. Peterson 1993; K. Bischoff & W. Kollatschny 1999; W. Kollatschny et al. 2018).

Assuming a linear response of a given emission line to continuum photons, the responding emission-line light curve can be described by the convolution of the continuum light curve with a transfer function (B. M. Peterson 1993):

$$\Delta L\ (v,\, t) = \int_{-\infty}^{\infty} \Psi(v,\, \tau)\ \Delta C(t - \tau)\ d\tau, \tag{1}$$

where $\Delta L(v,\, t)$ is the change in emission-line luminosity as a function of line-of-sight velocity v at time t relative to reference levels (e.g., the light-curve mean or median), $\Delta C(t - \tau)$ is the change in continuum light curve relative to the reference levels, and $\Psi(v,\, \tau)$ is the transfer function, or velocity-delay map, which describes the response of the emission line (after some time τ) to the continuum as a function of the line-of-sight velocity, v. Unraveling the transfer function (i.e., recovering the velocity-delay map), $\Psi(v,\, \tau)$, is the primary goal of reverberation mapping as the kinematics, geometry, and physics of the BLR are encoded within it (K. Horne et al. 2004).

The aforementioned reverberation mapping techniques involve measuring the lag across the entire emission line (i.e., the integrated lag), but it is also possible to measure the lag in different velocity bins. This idea of measuring the lag as a function of line-of-sight velocity, v, is called velocity-resolved reverberation mapping and allows one to make inferences about the kinematics of the BLR. Velocity-resolved reverberation mapping has unveiled a diversity of kinematics in the BLR (e.g., K. D. Denney et al. 2009a). For a simple BLR geometry, a virialized BLR will have longer lags in the bins at the line center, while having the shortest lags in the high-velocity wings. This is consistent with a virialized BLR interpretation since the lowest velocity gas should be further out. An infalling BLR will have the longest lags in the blueshifted bins and the shortest lags in the redshifted bins. This means that the gas on the far side (highest lags) is moving toward us (blueshifted) and the gas on the near side (shortest lags) is moving away from us (redshifted). An outflowing BLR will have the longest lags in the redshifted bins and the shortest lags in the blueshifted bins. This means that the gas on the far side (longest lags) is moving away from us (redshifted) and the gas on the near side (shortest lags) is moving toward us (blueshifted). Another signature that arises from velocity-resolved reverberation mapping is the presence of an "M" shape in the lags as a function of line-of-sight velocity. This M shape has been found in various emission lines previously such as Hβ, Hγ, and Lyα (L. Pei et al. 2017; K. Horne et al. 2021; K.-X. Lu et al. 2022). This M-shaped structure can be interpreted as a flat disk or spherical BLR where the illuminating source is emitting isotropically (L. Pei et al. 2017; K.-X. Lu et al. 2022) or an inclined Keplerian disk (K. Horne et al. 2021). Recent papers use dynamical models to infer additional details of the BLR kinematics and geometry from velocity-resolved reverberation mapping (L. Villafaña et al. 2022; Z. Stone et al. 2024, in preparation).

Velocity-resolved reverberation mapping requires a data set that has a high signal-to-noise ratio (SNR), high cadence, high spectral resolution, and a lengthy observation campaign. As such, the AGN that have had this analysis applied to them has been limited to a small sample of nearby Seyfert 1 AGN (M. C. Bentz et al. 2009, 2010b, 2021; K. D. Denney et al. 2009b; A. J. Barth et al. 2011; C. J. Grier et al. 2013; G. De Rosa et al. 2015, 2018; P. Du et al. 2016; S.-S. Li et al. 2022; K.-X. Lu et al. 2022; V. U et al. 2022). These previous efforts were single-target based, whereas the multiobject, long-duration, and many-epoch spectroscopic monitoring campaign of the Sloan Digital Sky Survey (SDSS) Black Hole Mapper Reverberation Mapping (BHM-RM) Project represents an opportunity to dramatically expand this analysis to a large set of quasars.

Using simple models (i.e., measuring the lag as a function of line-of-sight velocity) can illuminate inferences about the kinematics of the BLR (e.g., V. U et al. 2022), but in order to get a more complete view of the structure and kinematics of the BLR one must model it. There are two independent approaches for this kind of analysis: (1) through forward modeling (`CARAMEL`, A. Pancoast et al. 2011, 2014; `BRAINS`, Y.-R. Li et al. 2013, 2018), which uses a set of self-consistent models to explore the parameter space to find the solution that best matches the data or (2) through an inverse problem (`MEMECHO`, K. Horne 1994), which extracts the transfer function directly from the data. `MEMECHO` has been used to model a number of previous objects (M. C. Bentz et al. 2010a; C. J. Grier et al. 2013; M. Xiao et al. 2018; K. Horne et al. 2021), and it finds diverse kinematic signatures of the BLR gas. In future work, Z. Stone et al. (2024, in preparation) will show full dynamical modeling of RM160 using `BRAINS`.

In this work, we apply velocity-resolved reverberation mapping techniques to the luminous quasar RM160 to evaluate the phenomenological model proposed in L. B. Fries et al. (2023) and gain further insight into its kinematics and structure. Section 2 describes the properties of RM160, the spectroscopic observations, and the photometric observations used in this study. Section 3 describes the process of measuring the integrated time delays. Section 4 describes the process of measuring the velocity-resolved time delays. Section 5 describes our interpretation of the data. Finally, Section 6 summarizes our results.

Throughout this work, we assume a Lambda cold dark matter (ΛCDM) cosmology with $\Omega_\Lambda = 0.7$, $\Omega_{\rm M} = 0.3$, and $H_0 = 70$ km s^{-1} Mpc^{-1}.

2. Observations

2.1. Properties of RM160

RM160 is a luminous quasar located at R.A. = $14^{\rm h}10^{\rm m}41\overset{\rm s}{.}2$ and decl. = $53°18'48\overset{''}{.}995$ (J2000) with $z = 0.359$. There are previously measured reverberation mapping lags for RM160. C. J. Grier et al. (2017) found an observed-frame Hβ lag of $\tau_{{\rm H}\beta,{\rm obs}} = 31.3^{+8.1}_{-4.1}$ days and an observed-frame Hα lag of $\tau_{{\rm H}\alpha,{\rm obs}} = 27.7^{+5.3}_{-4.7}$ days using the 2014 spectroscopic data of RM160. Y. Homayouni et al. (2020) found an observed-frame Mg II lag of $\tau_{\rm Mg\,II,obs} = 144.7^{+24.7}_{-22.6}$ days for RM160 using the 2014–2017 spectroscopic data. C. J. Grier et al. (2017) also computed a black hole mass of $(M_{\rm BH}/10^7 M_\odot) = 7.0^{+1.7}_{-1.3}$ using the Hβ reverberation mapping results. We expand to 10 yr of spectroscopic monitoring and go beyond these integrated lags to perform velocity-resolved reverberation mapping.

2.2. BHM-RM/SDSS-RM Spectroscopy

The spectroscopic data were taken by the Sloan Digital Sky Survey Reverberation Mapping (SDSS-RM) project from 2014 to 2020 (Y. Shen et al. 2015, 2019) and the BHM-RM project from 2021–present (J. R. Trump et al. 2024, in preparation). The SDSS-RM survey was a part of the third (D. J. Eisenstein et al. 2011) and fourth (M. R. Blanton et al. 2017) iterations of the SDSS (D. G. York et al. 2000). The BHM-RM survey is a part of the fifth iteration (J. Kollmeier et al. 2019) of SDSS.

The data from both SDSS-RM and BHM-RM were taken using the plate-based, fiber-fed SDSS BOSS spectrograph (S. A. Smee et al. 2013) and the robotic focal plane system (FPS)-based spectrograph (C. Sayres et al. 2022) on the 2.5 m SDSS telescope (J. E. Gunn et al. 2006) at Apache Point Observatory in Sunspot, New Mexico. The plate-based data were taken from 2014 to 2021, while the FPS data were taken from 2022–present. There are irregularities between the cadences for a given year due to weather, SDSS scheduling priorities, instrument upgrades between successive generations of SDSS, and issues arising from the COVID-19 pandemic. There is a difference in spectrophotometric precision between SDSS-RM (3%; Y. Shen et al. 2015, 2019) and BHM-RM (5%; J. R. Trump et al. 2024, in preparation). The SDSS-RM (SDSS-III and SDSS-IV) data were reduced using the v5_13_0 version of idlspec2d (A. S. Bolton et al. 2012), which is the BOSS spectroscopic reduction pipeline. The BHM-RM data were reduced using the v6_0_9 version of idlspec2d (S. Morrison et al. 2024, in preparation).

In order to obtain light curves of the Mg II, Hβ, and Hα emission lines, we integrated the flux contained within each line after subtracting an (epoch-dependent) local continuum, as described in detail in Section 3.4 of L. B. Fries et al. (2023). We also obtained line widths of the rms spectra of each emission line using the first moment of the line profile, which is also described in Section 3.4 of L. B. Fries et al. (2023).

2.3. Photometry

Our continuum light curve consists of g- and i-band photometry from the Steward Observatory's 2.3 m Bok telescope and the 3.6 m Canada–France–Hawaii Telescope (CFHT), which span from 2014 to 2017 (see K. Kinemuchi et al. 2020 for more details regarding the photometry from Bok and CFHT). Additionally, it consists of g-, r-, and i-band photometry from Pan-STARRS from 2010 to 2013 (H. A. Flewelling et al. 2020) and from the Zwicky Transient Facility (ZTF; F. J. Masci et al. 2019) from 2018 to 2023. It also includes synthetic SDSS r-band photometry from 2014 to 2019. The aforementioned photometric observations were merged together using the public code `PyCali` (Y.-R. Li et al. 2014) to account for instrumental differences. For more information on the merging process see Section 3.2 of Y. Shen et al. (2024). Figure 1 shows the continuum light curve for RM160.

3. Integrated Lags

3.1. Lag Measurement Methodology

We use the photometric light curve as the driving light curve (continuum) in our reverberation mapping analysis and the emission-line light curves as the responding light curves. We use `PyROA` (F. R. Donnan et al. 2021) to fit the light curves in order to recover the emission-line lags.[26] `PyROA` uses a Bayesian Markov Chain Monte Carlo (MCMC) approach to model quasar variability with a running optimal average (ROA), where the optimal average is a weighted average with the weights being the inverse variance. The ROA is applied within a window function whose width can be specified. The window function acts as a filter whereby the impact of data points far from the point of interest are reduced. For a continuous monitoring program (i.e., data with no seasonal gaps) a smaller window function width is optimal, whereas for a monitoring program like SDSS-RM/BHM-RM with seasonal gaps, a larger window function width is optimal.

`PyROA` offers unique functionality compared to more traditional lag measuring methods. In particular, `PyROA` lets the user fit multiple responding light curves at once (where the driving light curve is constrained with respect to all of the responding light curves), and allows the user the ability to choose different shapes for the delay distribution, or transfer function, in the fit. Additionally, `PyROA` offers the user the ability to input an extra error rescaling parameter (σ), which has been demonstrated to recover lags better than `JAVELIN` when

---

[26] https://github.com/FergusDonnan/PyROA

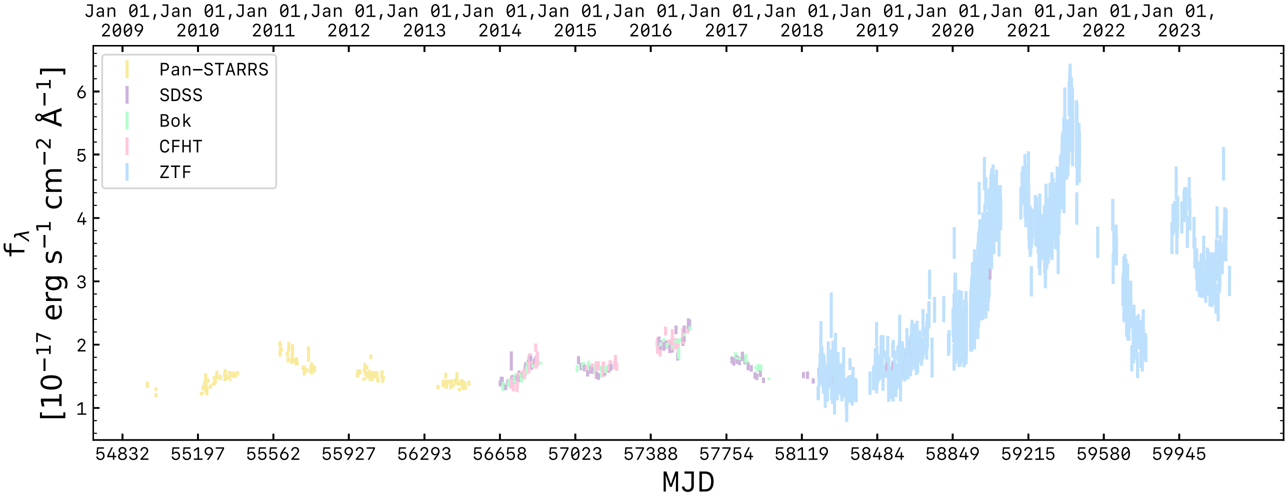

Figure 1. Photometric light curve for RM160, demonstrating the long baseline of our photometric coverage. The photometric (continuum) light curve is comprised of data from Bok (green points), CFHT (pink points), Pan-STARRS (yellow points), SDSS (purple points), and the ZTF (blue points). These data include *gri* photometry and been merged together to account for instrumental differences using `PyCali` (Y.-R. Li et al. 2014).

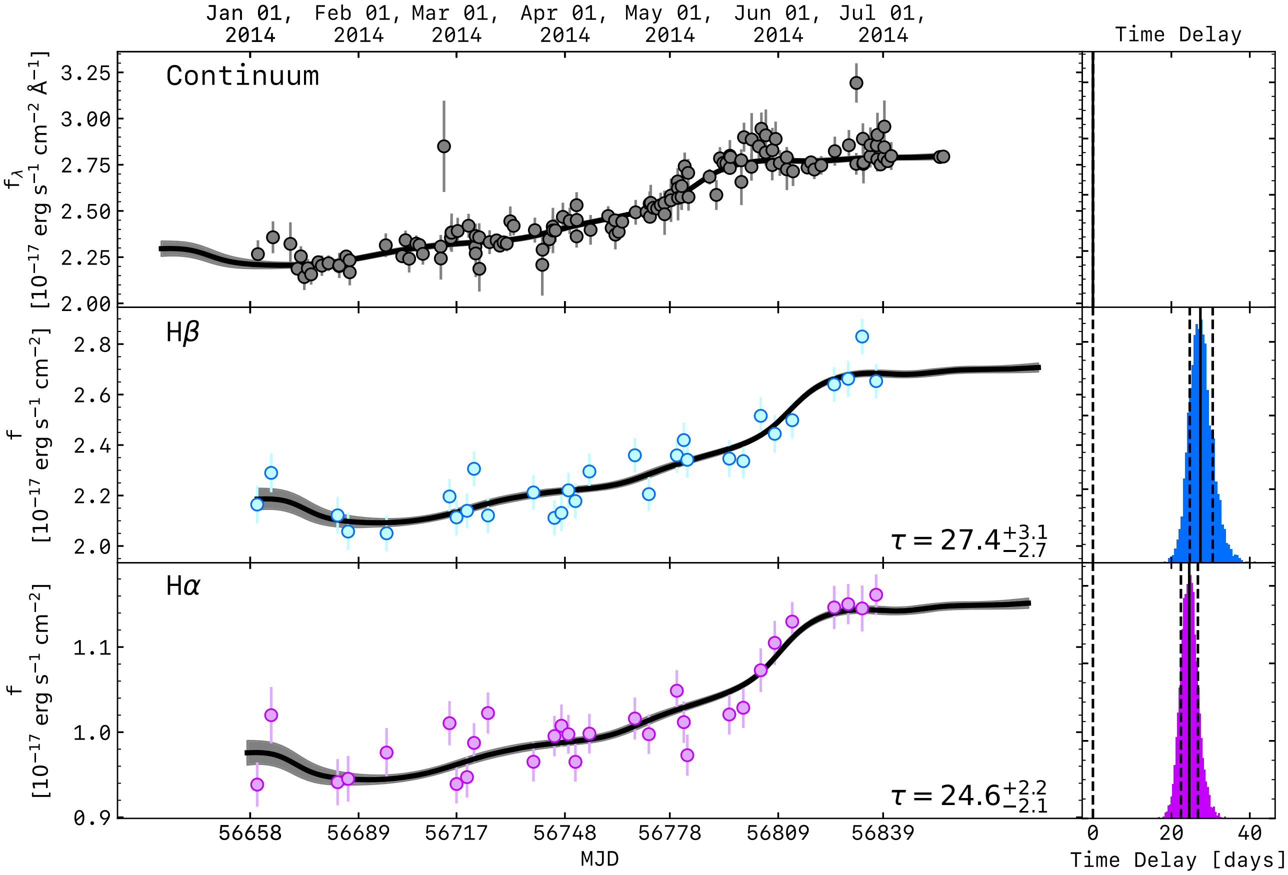

Figure 2. 2014 Balmer light curves with the best-fit `PyROA` model overlaid as a solid black line with the corresponding error envelope. The top, middle, and bottom panels show the continuum, Hβ, and Hα light curves, respectively. The best-fit time delay along with its corresponding errors are on the bottom right of the Hβ and Hα light-curve panels. The posterior distribution for the time delay is on the right panel of each responding light curve where the median value and 68th percentile errors are the solid and dashed lines, respectively. We also show, on the right-hand panels, a vertical dashed line at zero time delay for reference. We find an Hβ time delay of $27.4^{+3.1}_{-2.7}$ days and an Hα time delay of $24.6^{+2.2}_{-2.1}$ days, which are consistent with the `JAVELIN` time delays computed in C. J. Grier et al. (2017).

the flux errors are underestimated (F. R. Donnan et al. 2021). `PyROA` has been applied recently in measuring accretion disk lags in PG 1119+120 (F. R. Donnan et al. 2023) and Mrk 817 (E. M. Cackett et al. 2023) as well as broad-line lags for a catalog of 849 SDSS-RM broad-line quasars (Y. Shen et al. 2024).

`PyROA` lets the user input lower and upper limits to uniform priors, which are hard limits, on five parameters: A (rms flux of each light curve, in units of rms flux to the median absolute deviation, or MAD, light curve), B (mean flux of each light curve, in units of mean flux to the median light curve), τ (the time delay of each light curve, in units of days), Δ (the width of

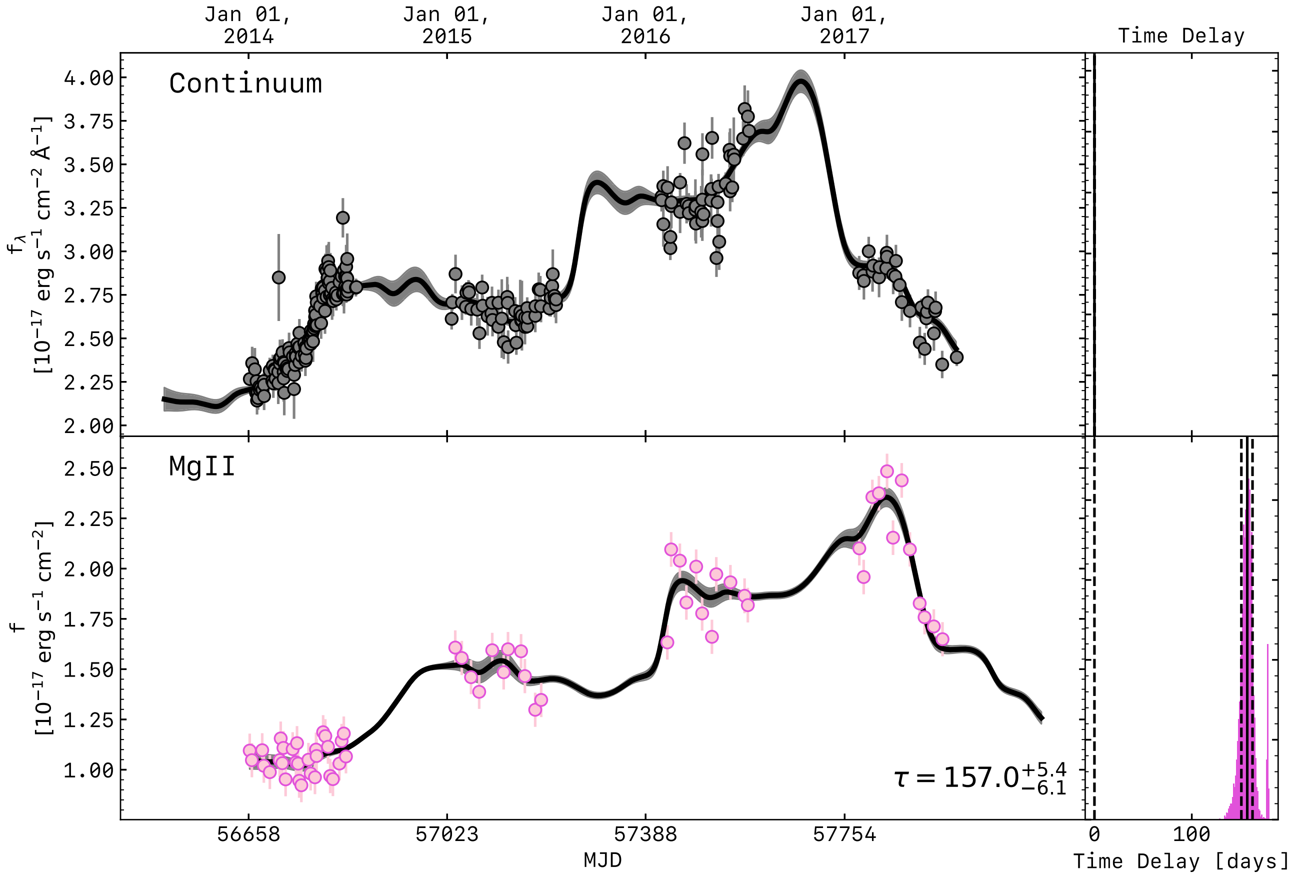

Figure 3. 2014–2017 Mg II light curve with the best-fit `PyROA` model overlaid as a solid black line with the corresponding error envelope. The top panel shows the continuum, while the bottom panel shows the Mg II light curve. The best-fit time delay along with its corresponding errors are on the bottom right of the Mg II light-curve panel. The posterior distribution for the time delay is on the right panel of each responding light curve where the median value and 68th percentile errors are the solid and dashed lines, respectively. We also show, on the right-hand panels, a vertical dashed line at zero time delay for reference. We find an Mg II time delay of $157.0^{+5.4}_{-6.1}$ days, which is consistent with the `JAVELIN` time delay computed in Y. Homayouni et al. (2020).

Table 1
Comparison of the 2014 Balmer and 2014–2017 Mg II Integrated Lag Measurements between `JAVELIN` and `PyROA`

Method	$\tau_{\text{Mg II}}$	$\tau_{\text{H}\beta}$	$\tau_{\text{H}\alpha}$
`JAVELIN`	$144.7^{+24.7}_{-22.6}$	$31.3^{+8.1}_{-4.1}$	$27.7^{+5.3}_{-4.7}$
`PyROA`	$157.0^{+5.4}_{-6.1}$	$27.4^{+3.1}_{-2.7}$	$24.6^{+2.2}_{-2.1}$

Note. We find that both lag measurement methods recover the same results within the errors.

the window function of the ROA algorithm, in units of days), and σ (an extra error rescaling parameter, in units of flux). Our choice in the lower and upper limits to the uniform priors is listed below:[27]

1. A: [0.0, 2.0],
2. B: [0.0, 2.0],
3. τ: [0.0, 300.0],
4. Δ: [5.0, 50.0], and
5. σ: [0.0, 10.0].

For our `PyROA` fits, we first scale the responding light-curve flux to be on the same order of magnitude as the driving light curve, as this causes the fit to converge more quickly. We use a delta-function delay distribution shape. We find that the inclusion of an additional free parameter (i.e., more complex shapes of the delay distribution such as a Gaussian or log-Gaussian) leads to more degeneracies in the fit, which leads to larger uncertainties in the best-fit lags. Finally, we use 25,000 MCMC samples and discard the first 20,000 of them for burn-in in our fits.

3.2. Comparison to Previously Measured Lags

In order to motivate our usage of `PyROA`, we compare the results of `PyROA` with `JAVELIN`. The time delays of the BLR for RM160 have been studied previously (C. J. Grier et al. 2017; Y. Homayouni et al. 2020) on smaller timescales. These studies used `JAVELIN`, which models quasar variability with a damped random walk model with a top-hat transfer function shape. `PyROA` models quasar variability with an ROA algorithm, assumes no shape to the driving light curve, and allows the user to supply a range of transfer function shapes (delta function, Gaussian, log-Gaussian, truncated Gaussian, etc.). Furthermore, `PyROA` does a better job at dealing with seasonal gaps and aliasing over long baselines (see Section 4.2 in Y. Shen et al. 2024). For more detail on the usage of `JAVELIN` as it pertains to RM160, please see C. J. Grier et al. (2017) and Y. Homayouni et al. (2020).

---

[27] We note that the way the A and B priors are computed have changed from `PyROA` v3.1.0 to v3.2.0. For clarity, we have done this analysis on `PyROA` v3.2.0.

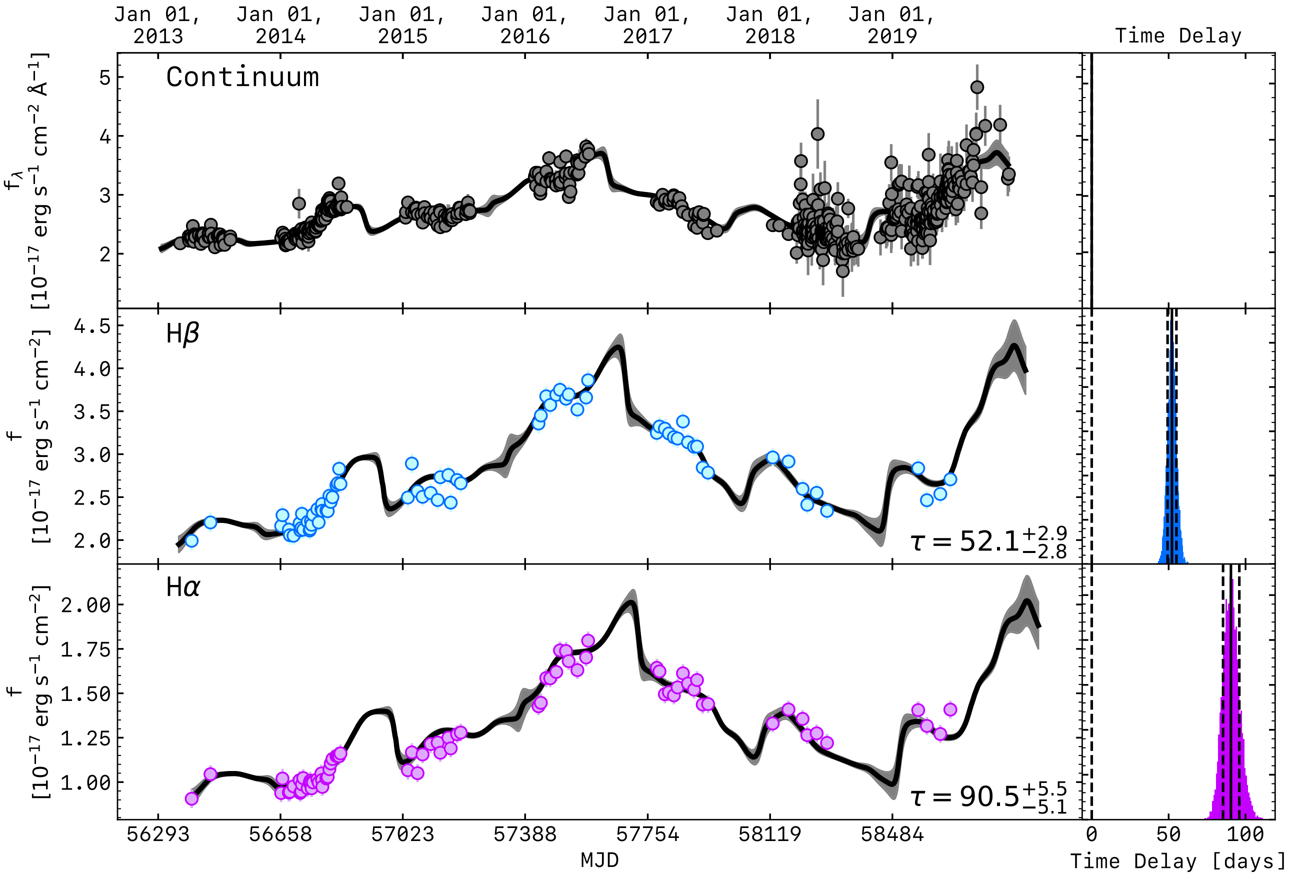

Figure 4. Low-state (2013–2019) Balmer light curves with the best-fit `PyROA` model overlaid as a solid black line with the corresponding error envelope. The top, middle, and bottom panels show the continuum, Hβ, and Hα light curves, respectively. The best-fit time delay along with its corresponding errors are on the bottom right of the Hβ and Hα light-curve panels. The posterior distribution for the time delay is on the right panel of each responding light curve where the median value and 68th percentile errors are the solid and dashed lines, respectively. We also show, on the right-hand panels, a vertical dashed line at zero time delay for reference. We find an Hβ time delay of $52.1^{+2.9}_{-2.8}$ days and an Hα time delay of $90.5^{+5.5}_{-5.1}$ days, which are longer than the time delays found in 2014 (Figure 2). This is likely due to the fact that the low state includes the moderate increase in flux from 2014 to 2017.

Using the emission-line light curves from the monitoring periods of C. J. Grier et al. (2017) and Y. Homayouni et al. (2020), we use `PyROA` to measure the lags for the Balmer (Hβ and Hα) lines and Mg II, respectively. Since `PyROA` allows for multiple responding light curves to be fit at once, we fit Hβ and Hα simultaneously. Our resultant fit from `PyROA` for the Balmer lines is shown in Figure 2. We find an observed-frame Hβ lag of $27.4^{+3.1}_{-2.7}$ days and an observed-frame Hα lag of $24.6^{+2.2}_{-2.1}$ days. This is consistent with the observed-frame Hβ and Hα lags from C. J. Grier et al. (2017) using `JAVELIN` of $31.3^{+8.1}_{-4.1}$ days and $27.7^{+5.3}_{-4.7}$ days, respectively. Our resultant fit from `PyROA` for Mg II is shown in Figure 3. We find an observed-frame Mg II lag of $157.0^{+5.4}_{-6.1}$ days. This is consistent with the observed-frame Mg II lag from Y. Homayouni et al. (2020) using `JAVELIN` of $144.7^{+24.7}_{-22.6}$ days. Table 1 shows a comparison between `PyROA` and `JAVELIN`. We find that the time delays measured by `PyROA` and `JAVELIN` agree within the uncertainties, validating our use of `PyROA` for measuring reverberation lags in this work. The `PyROA` errors are slightly smaller than `JAVELIN`. We anticipate this as due to a more well constrained fit by using multiple responding light curves to constrain the fit. Further discussion of `PyROA` and `JAVELIN` error comparison is given in F. R. Donnan et al. (2021).

3.3. Measuring the Integrated Lags

With the aim of understanding the structure of the BLR, we measure the time delays for each emission line using `PyROA`. In Figure 1, we see that the there is a long period of relatively low flux (i.e., a "low state") in the continuum from 2013 to 2019 and a rapid increase by a factor of >3 from 2019 to 2021. In our analysis, we seek to minimize the effects of nonreverberation variability of the BLR from line breathing, which is characterized by the correlation between flux and BLR emission radius resulting from the dramatic increases/decreases in the continuum flux. We avoid the contribution of nonreverberation variability to the measured lags by splitting the light curves into two regions: the low state from 2013 to 2019 and the "high state" from 2022 to 2023.

Since `PyROA` allows multiple responding light curves to be fit at once, we first run `PyROA` on all the emission lines (Mg II, Hβ, and Hα) for the low state. This allows the best-fit driving light-curve model to be constrained by all of the emission lines and is presumably the best way to constrain the driving light curve if the emission lines all respond in the same qualitative way to the continuum. However, we find that `PyROA` cannot compute good time delays while simultaneously fitting the Balmer line and Mg II light curves of RM160. We find that the best-fit `PyROA` driving light curve results in a poor fit to the Mg II light curve and even the Balmer lines have less reliable

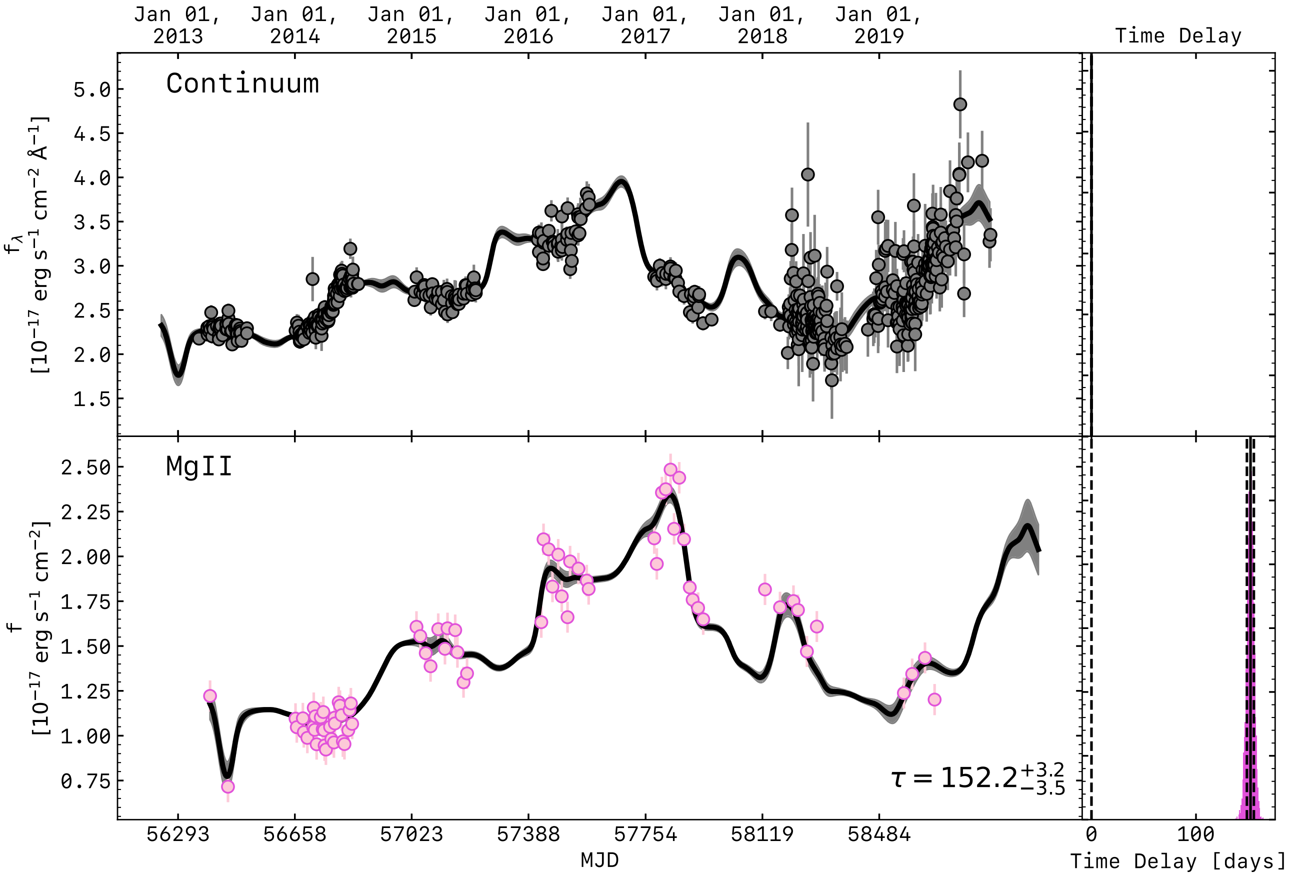

Figure 5. Low-state (2013–2019) Mg II light curve with the best-fit `PyROA` model overlaid as a solid black line with the corresponding error envelope. The top panel shows the continuum, while the bottom panel shows the Mg II light curve. The best-fit time delay along with its corresponding errors are on the bottom right of the Mg II light-curve panel. The posterior distribution for the time delay is on the right panel of each responding light curve where the median value and 68th percentile errors are the solid and dashed lines, respectively. We also show, on the right-hand panels, a vertical dashed line at zero time delay for reference. We find an Mg II time delay of $152.2^{+3.2}_{-3.5}$ days, which is consistent with the time delay computed during the 2014–2017 time period (Figure 3). This is likely due to the fact that both time periods include the same range of continuum and line flux.

time delays due being constrained by the qualitatively different Mg II light curve (see Section 3.4 for more details). We then run `PyROA` on the Balmer lines (both Hα and Hβ are fit simultaneously) and then Mg II separately.

Our `PyROA` best-fit model light curves for the low state are shown for the Balmer lines in Figure 4 and for Mg II in Figure 5. For the Balmer lines, we find a different mean time delay for both Hα and Hβ compared to the 2014 analysis. We find that the Hβ mean time delay increases by a factor of ∼2× and the Hα mean time delay increases by a factor of ∼2.5×. This increase is likely caused by the factor of ∼1.8× increase in flux from 2014 to 2016. For Mg II, we find a similar mean time delay comparing the low-state analysis to the 2014–2017 analysis. This is due to the 2014–2017 analysis capturing the modest increase in flux, so a similar mean time delay is expected.

Our `PyROA` best-fit model light curves for the high state are shown for the Balmer lines in Figure 6. For the Balmer lines, we find a different mean time delay for both Hβ and Hα from the 2014 analysis in C. J. Grier et al. (2017) and a slight difference in our low-state analysis. This is to be expected from line breathing, where an increase in continuum luminosity will yield a longer mean time delay. We observe an ∼1.14× increase in the Hβ mean time delay from the low state to high state, resulting in a 1.61σ difference using the average of the asymmetric error bars. We observe an ∼0.09× decrease in the Hα mean time delay from the low state to high state, resulting in a 1.27σ difference using the average of the asymmetric error bars. This decrease in the Hα mean time delay from a period of low flux to high flux is unexpected from photoionization physics since a photoionization-bounded BLR should show longer lags during periods of high flux (A. J. Barth et al. 2015; S. Wang et al. 2020). In contrast to the Balmer lines, we find that the Mg II light curve is poorly constrained in the high state owing to a qualitatively different response to the continuum.

3.4. *The Anomalous Behavior of Mg II*

Qualitatively, the Mg II line appears to reverberate in a different way than the Balmer lines after the increase in the received continuum luminosity in 2021. Since we are attempting to simultaneously fit all three emission-line light curves from the same driving light curve, the Balmer lines have considerably worse fits due to being constrained by the qualitatively different Mg II light curve. We find that the Mg II response is similar to the Balmer lines in the low state, but not similar in the high state. We also see this in the kinematics of the lines (L. B. Fries et al. 2023).

The qualitative differences between the Mg II light curve and the Balmer lines could be due to the fact that the spectrophotometric reliability in the bluest wavelengths for SDSS-RM/BHM-RM is poor (see Figure 20 in Y. Shen et al. 2015). However, the Mg II response being similar in the low state, but

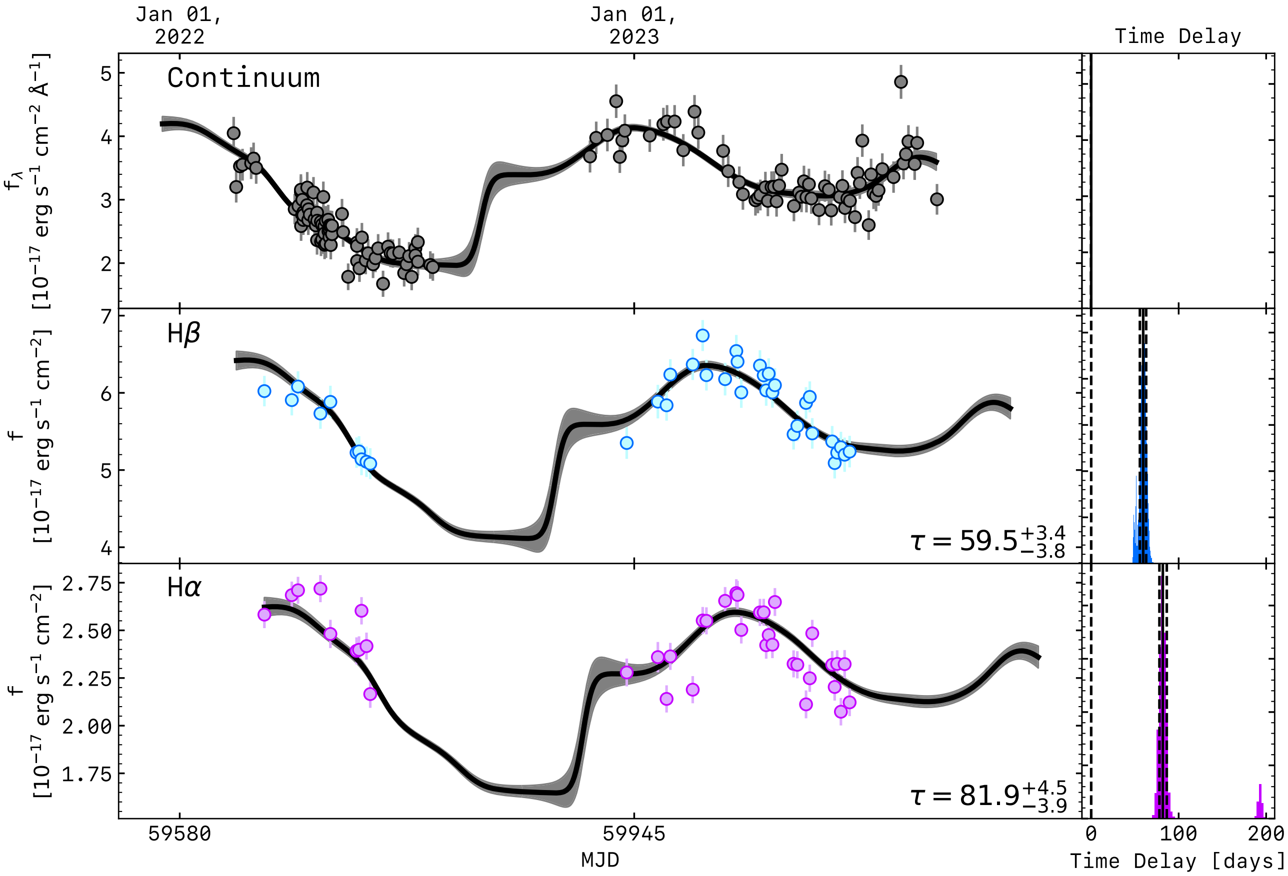

Figure 6. High-state (2022–2023) Balmer light curves with the best-fit `PyROA` model overlaid as a solid black line with the corresponding error envelope. The top, middle, and bottom panels show the continuum, Hβ, and Hα light curves, respectively. The best-fit time delay along with its corresponding errors are on the bottom right of the Hβ and Hα light-curve panels. The posterior distribution for the time delay is on the right panel of each responding light curve where the median value and 68th percentile errors are the solid and dashed lines, respectively. We also show, on the right-hand panels, a vertical dashed line at zero time delay for reference. We find an Hβ time delay of $59.5^{+3.4}_{-3.8}$ days and an Hα time delay of $81.9^{+4.5}_{-3.9}$ days. The Hβ time delay in the high state is longer than the Hβ time delay in the low state. This is consistent with the general expectation of a photoionized BLR. In other words an increase in flux will push the optimal emission radius (BLR radius) further out. However, we observe the opposite in the case of Hα, where the Hα low state has a higher time delay than the high state.

dissimilar in the high state suggests this is not an issue with the blue side of the spectrograph. The differences also could be due to the fact that Mg II is close to the dust-sublimation radius and the delay distribution is being truncated due to dust sublimation in the outer BLR (A. Baskin & A. Laor 2018; S. Wang et al. 2020). Another reason could be due to the fact that Mg II includes significant contribution from collisional excitation in addition to photoionization, which dominates for the Balmer lines (H. Guo et al. 2020). This added contribution of collisional excitation could lead to a BLR geometry with a broader radial extent and a more complicated response than simple line breathing. Figure 7 shows the high state Mg II best-fit `PyROA` light curve for clarity. Due to these added complications, we omit the Mg II line for the rest of our analysis.

4. Resolving the Kinematics of the Broad-line Region

4.1. Velocity-resolved Lags

In order to probe the kinematics of the BLR, we measure the velocity-resolved response using `PyROA` for individual velocity segments of each emission line. Following K. D. Denney et al. (2009a), M. C. Bentz et al. (2009), C. J. Grier et al. (2013), and V. U et al. (2022), we use two schemes to divide the emission line into eight individual velocity segments in order to determine any potential effects of binning on the measured lags. The two schemes are as follows: (i) velocity segments of equal rms flux, and (ii) velocity segments of equal rms velocity. Tables 2 and 3 show the breakdown for the eight partitions for equal rms flux and equal rms velocity, respectively. Throughout this work, we use the equal rms flux bins for all of our interpretations, although we confirmed that the equal rms velocity bins exhibit the same general trends for each of the velocity-resolved lag profiles (VRLPs).

We determine the integrated flux in each partition using the method described in detail in L. B. Fries et al. (2023). Briefly, we use a nonparametric method (see Section 3.4 of L. B. Fries et al. 2023 for more detail) to determine the integrated broad-line flux from the continuum-subtracted and narrow-line-subtracted spectra. We do this for the partitions for each emission line shown in Tables 2 and 3 for all epochs, yielding eight different light curves with 153 data points for each emission line for each choice of partitioning.

For our velocity-resolved analysis, we use the same `PyROA` priors and methodology as we did for our integrated analysis in Section 3.1. However, we simultaneously fit the velocity-resolved light curves of each emission line along with the integrated light curve, resulting in nine responding light curves in the fit. We found that fitting the velocity-resolved light curves separately and simultaneously gave the same results,

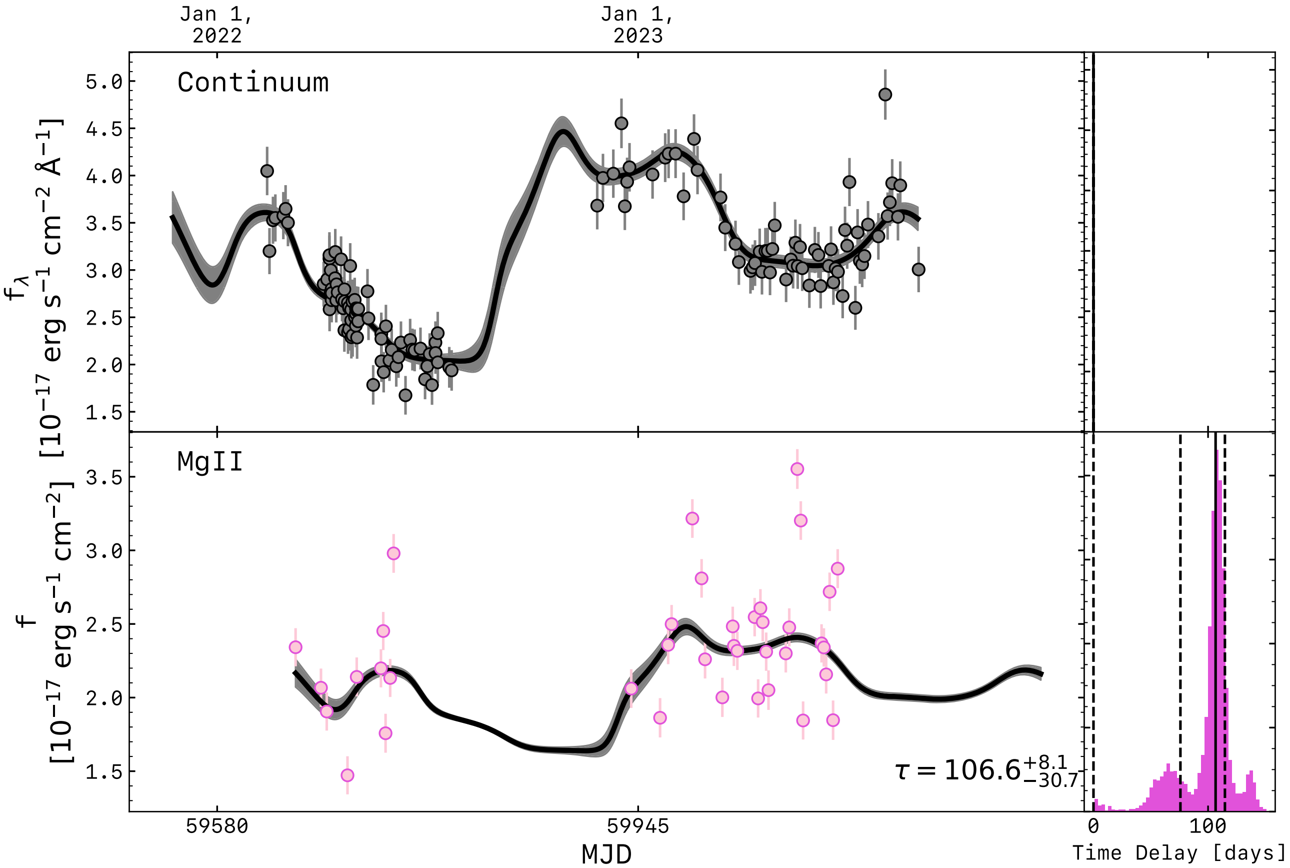

Figure 7. High-state (2022–2023) Mg II light curve with the best-fit `PyROA` model overlaid as a solid black line with the corresponding error envelope. The top and bottom panels show the continuum, Mg II light curves, respectively. The best-fit time delay along with its corresponding errors are on the bottom right of the Mg II light-curve panel. The posterior distribution for the time delay is on the right panel of the responding light curve where the median value and 68th percentile errors are the solid and dashed lines, respectively. We also show, on the right-hand panels, a vertical dashed line at zero time delay for reference. We find that the Mg II high state is not well constrained by the `PyROA` model.

Table 2
The Wavelength Range and Characteristic Velocity of the Eight Equal rms Flux Bins Used in Our Velocity-resolved Reverberation Mapping Analysis

	Mg II			Hβ			Hα		
Partition	$\langle v\rangle_f$	$\lambda_{\rm low}$	$\lambda_{\rm high}$	$\langle v\rangle_f$	$\lambda_{\rm low}$	$\lambda_{\rm high}$	$\langle v\rangle_f$	$\lambda_{\rm low}$	$\lambda_{\rm high}$
1	−1.98	3754.05	3793.15	−1.49	6544.85	6596.29	−1.78	8820.63	8900.19
2	−0.46	3793.15	3802.77	−0.27	6596.29	6609.97	−0.38	8900.19	8920.71
3	0.12	3802.77	3808.90	0.22	6609.97	6619.11	0.12	8920.71	8933.04
4	0.57	3808.90	3814.16	0.59	6619.11	6626.73	0.50	8933.04	8943.33
5	0.97	3814.16	3819.44	0.93	6626.73	6634.37	0.84	8943.33	8953.64
6	1.42	3819.44	3825.60	1.31	6634.37	6643.54	1.18	8953.64	8963.95
7	1.96	3825.60	3833.54	1.77	6643.54	6655.79	1.59	8963.95	8978.41
8	2.92	3833.54	3860.11	2.70	6655.79	6697.30	2.29	8978.41	9042.47

Note. $\langle v\rangle_f$ is the flux-weighted velocity of the bin in units of 10^{-3} km s^{-1}, $\lambda_{\rm low}$ is the lower bound observed-frame wavelength of the bin in units of angstrom, and $\lambda_{\rm high}$ is the upper bound observed-frame wavelength of the bin in units of angstrom.

and chose to fit all of them simultaneously to save computation time. Therefore, due to the velocity-resolved light curves being fit simultaneously with the integrated light curve, the integrated lags reported in this section will differ from those in Section 3.3.

We show our VRLPs for Hβ and Hα in Figures 8 and 9, respectively (we show the best-fit `PyROA` light curves for our velocity-resolved analysis in Appendix A). Each figure shows the VRLPs for both the high and low states as denoted in Section 3.3. Both Hα and Hβ have high-SNR light curves and we expect that the measured lag uncertainties are dominated by time resolution rather than the flux uncertainties. We note that the rms broad-line profiles of the high-state Hβ and high- and low-state Hα are redshifted from the systemic redshift. These radial-velocity shifts for the Balmer lines are suggestive of a bulk inflow of the BLR gas with a gradient of higher velocity at smaller radii, as described in detail in L. B. Fries et al. (2023). A VRLP of the highest time delay at the zero velocity and lowest time delays at the high-velocity wings is consistent with virialized motion of the BLR. In this interpretation, the closest gas (low time delays) is moving fastest as is expected from the virial theorem ($v \sim R^{-1/2}$). A VRLP with the longest lags in the

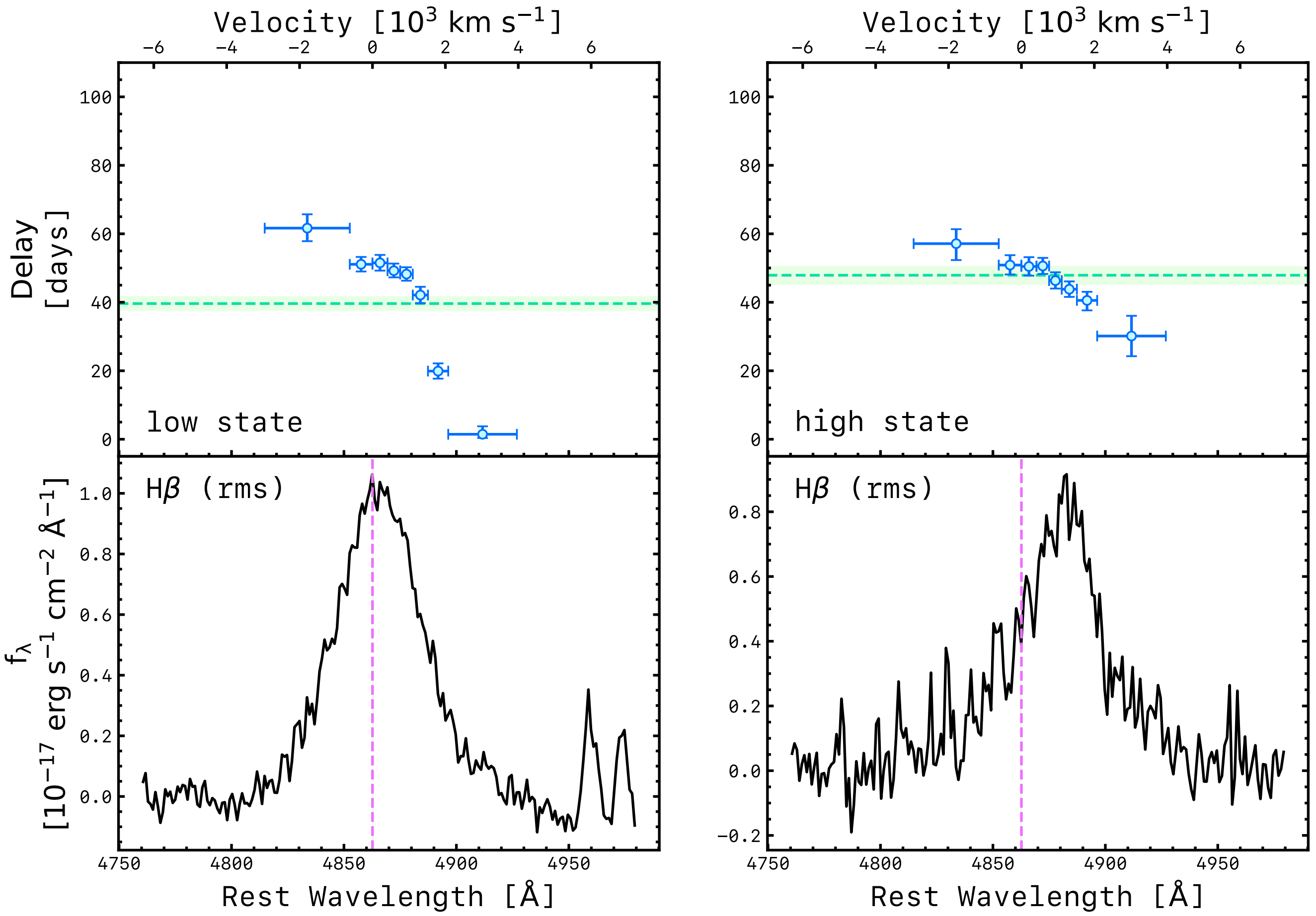

Figure 8. VRLP for Hβ. The left side presents the lags measured from the low state (2013–2019) while the right side presents the lags measured from the high state (2022–2023). The top panels are the VRLP where the dashed green line represents the integrated time delay and the shaded green region represents $\pm 1\sigma$ errors in the integrated time delay. For each point, the x-axis error bars represent the velocity bin as denoted in Table 2 and the y-axis error bars represent the error in the time delay computed from `PyROA`. The bottom panels are the rms spectrum for each state. The vertical dashed magenta line represents the systemic redshift for Hβ. The velocity-resolved lags in both the low state and the high state are consistent with an inflowing BLR.

blue wing of the emission line and shortest time delays in the red wing of the emission line indicates an infalling BLR. A VRLP with the longest lags in the red wing and the shortest lags in the blue wing indicates an outflowing BLR. A simple model for understanding these nonvirial kinematics is that in the inflowing scenario the far side (longest lags) of the BLR is moving toward us (blueshifted), while the near side (shortest lags) of the BLR is moving away from us (redshifted). In the outflowing scenario the far side (longest lags) is moving away from us (redshifted), while the near side (shortest lags) is moving toward us (blueshifted; A. Pancoast et al. 2011, 2014).

The Hβ VRLP for the low state has higher lags at bluer wavelengths and decreases toward redder wavelengths, which is consistent with an infalling BLR. This is consistent with the suggestion of inflow from the extremely red radial-velocity shifts in the Hβ broad line described by L. B. Fries et al. (2023). The high state also exhibits this same infalling kinematic signature. An interesting observation is that the slope of the infalling signature from the high state to the low state seems to decrease even while both appear to be consistent with an infalling signature.

For Hα, the low state has a profile that is marginally consistent with virial motion whereby the highest lags are near the line center, while the lowest lags are in the high-velocity wings. However, the high state has a different shape and is instead marginally consistent with an inflowing BLR whereby the lowest lags are on the red side and the highest lags are on the blue side.

While Hβ appears to have "stable" or consistent BLR kinematics from the low state to the high state, Hα transitions from a virialized structure in the low state to a signature of inflow in the high state. This suggests that there are some physical processes in the slightly outer part of the BLR changing the inferred kinematics.

5. Discussion

5.1. Differences in the Balmer Lines

Figures 8 and 9 demonstrate that the inferred kinematics from our velocity-resolved reverberation mapping analysis yields different results between the Balmer lines in the low state despite being produced by the same emission mechanism. Hβ shows a signature of an infalling BLR, while Hα shows a virialized signature. However, the profiles are more similar in the high state, but there is still anomalous behavior in that the Hα lag becomes shorter despite the higher continuum luminosity, while the Hβ lag becomes longer. Higher orders of Balmer lines (such as Hγ) for RM160 have low SNR and are unable to be used to measure velocity-resolved as well as integrated lags.

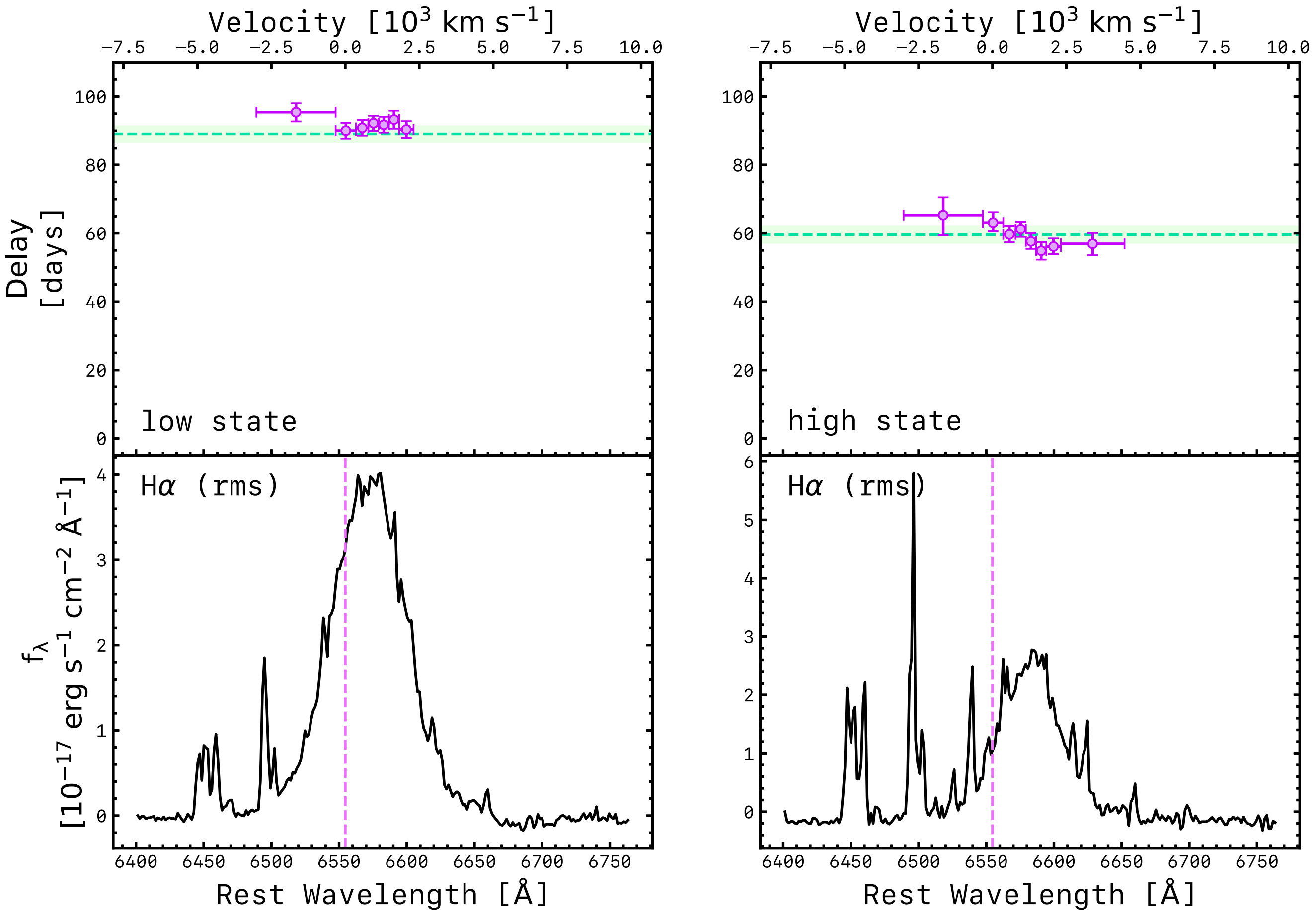

Figure 9. VRLP for Hα. The left side represents the low state (2013–2019) while the right side represents the high state (2022–2023). The top panels are the VRLP where the dashed green line represents the integrated time delay and the shaded green region represents $\pm 1\sigma$ errors in the integrated time delay. For each point, the x-axis error bars represent the velocity bin as denoted in Table 2 and the y-axis error bars represent the error in the time delay computed from `PyROA`. The bottom panels are the rms spectrum for each state. The spikes to the left of the Hα profile in both the low and high states are improperly subtracted skylines. The vertical dashed magenta line represents the systemic redshift for Hα. The velocity-resolved lags in the low state are consistent with a virialized BLR, while in the high state the velocity-resolved lags are consistent with an inflowing BLR. This change in velocity-resolved lags is consistent with a kinematically stratified BLR whereby the low state is probing more distant, virial gas, while the high state is probing more nearby, inflowing gas. The integrated lags from the high state are roughly consistent to the integrated lag of both the low and high state of Hβ where there is also inflowing kinematics.

Table 3
The Wavelength Range and Characteristic Velocity of the Eight Equal rms Velocity Bins Used in Our Velocity-resolved Reverberation Mapping Analysis

	Mg II			Hβ			Hα		
Partition	$\langle v\rangle_f$	$\lambda_{\rm low}$	$\lambda_{\rm high}$	$\langle v\rangle_f$	$\lambda_{\rm low}$	$\lambda_{\rm high}$	$\langle v\rangle_f$	$\lambda_{\rm low}$	$\lambda_{\rm high}$
1	−2.95	3760.05	3773.52	−2.48	6543.90	6563.18	−3.83	8789.64	8823.10
2	−1.86	3773.52	3787.00	−1.67	6563.18	6582.46	−2.85	8823.10	8856.56
3	−0.76	3787.00	3800.47	−0.76	6582.46	6601.74	−1.59	8856.56	8890.03
4	0.25	3800.47	3813.94	0.12	6601.74	6621.02	−0.41	8890.03	8923.49
5	1.26	3813.94	3827.42	0.93	6621.02	6640.30	0.59	8923.49	8956.95
6	2.28	3827.42	3840.89	1.74	6640.30	6659.57	1.59	8956.95	8990.41
7	3.29	3840.89	3854.37	2.63	6659.57	6678.85	2.63	8990.41	9023.88
8	4.41	3854.37	3867.84	3.54	6678.85	6698.13	3.82	9023.88	9057.34

Note. $\langle v\rangle_f$ is the flux-weighted velocity of the bin in units of 10^{-3} km s^{-1}, $\lambda_{\rm low}$ is the lower bound observed-frame wavelength of the bin in units of angstrom, and $\lambda_{\rm high}$ is the upper bound observed-frame wavelength of the bin in units of angstrom.

Both photoionization modeling and observations have shown that Hα is observed from slightly further out in the BLR due to radial stratification and optical depth effects (H. Netzer 1975; M. J. Rees et al. 1989; K. T. Korista & M. R. Goad 2004; M. C. Bentz et al. 2010b). The BLR has different kinematics at different radii. The Hα reverberation profile generally probes more distant gas (with potentially different kinematics) compared to the smaller-radius gas probed by Hβ. Due to this, we postulate that the different kinematic signatures at different radii in the low state indicates a strong kinematic gradient in the BLR gas.

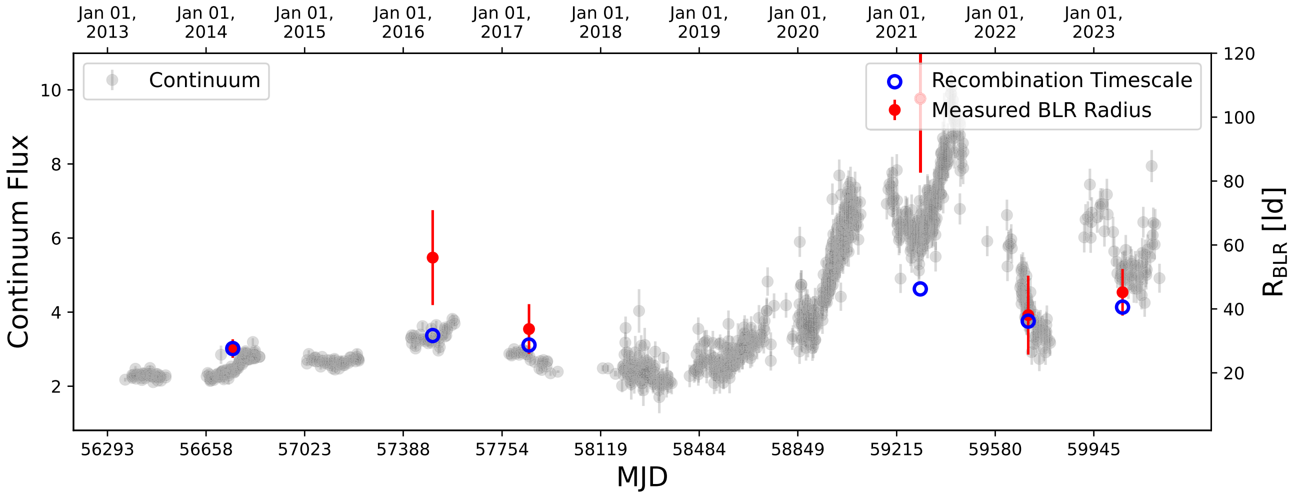

Figure 10. Measured Hβ BLR radii and expected recombination timescale over plotted onto the continuum light curve. The open, blue circles show the recombination timescale expectation, the solid, red circles are the measured BLR radii, and the gray points are the continuum light curve. The points are all normalized such that they overlap in 2014. The measured BLR radii follow from our cross-correlation analysis in a given year, while the recombination timescale expectation assumes that the lag is proportional to $\sqrt{f_{\rm cont}}$. We find that the recombination timescale expectation and the measured BLR radii are the same within the uncertainties, which means the recombination timescale expectation holds for RM160.

5.2. Kinematic Evolution

Figure 9 demonstrates that there is a marginal evolution of kinematics for the Hα line throughout the monitoring period. In the low state, we find a velocity-resolved response consistent with virialized motion of the BLR gas, while in the high state we find a velocity-resolved response indicating an infalling motion of the BLR gas. The Hβ response does not exhibit the same dramatic evolution, with only modest differences in the velocity-resolved lags that are consistent with inflow in both the low and high states. This modest kinematic evolution of Hα could plausibly be due to some physical process within the outer BLR since Hα has been shown to be slightly further out.

This evolution of the inferred Hα kinematics from virial to inflowing is plausibly due to a dynamically stratified BLR. In Figure 9, we see that the integrated lag during the low state is ∼90 days, while the integrated lag during the high state is ∼60 days. If we compare these integrated lags for Hα to those of Hβ in Figure 8, we see that both the low state and the high state for Hβ have integrated lags of ∼40–50 days, which is comparable to the Hα high state. This would mean that during the low state, Hα is illuminating the virialized outer part of the BLR, while then illuminating the close, infalling gas during the high state. The decrease in the integrated Hα lag from a period of low continuum luminosity to high continuum luminosity is somewhat paradoxical in the framework of a photoionization-bounded BLR.

5.3. Adjustment Time of the Broad-line Region

Recent velocity-resolved reverberation mapping studies have unveiled similar evolution in the BLR kinematics. M. Xiao et al. (2018) used archival AGN Watch data for NGC 5548 to produce Hβ velocity-delay maps with `MEMECHO` (K. Horne 1994).[28] They found an evolution of kinematics with transitions between a virial BLR and an inflowing BLR, suggesting that the shrinking of the BLR might correlate to inflow dynamics. Y.-J. Chen et al. (2023) studied the Hβ velocity-resolved response from NGC 4151 for multiple seasons over ∼2 decades. They found that in four of their seasons (1996, 1998, 2018, and 2021) the Hβ response was virial with possibly a contribution from inflow/outflow, while in the last season (2022) they found an outflowing BLR. They examined the velocity-resolved response with respect to the photometric light curve and found that the BLR is virial and inflowing during periods of rising continuum luminosity and that the BLR is virial and outflowing in periods of falling continuum luminosity. They posited that the rise in luminosity could be the result of enhanced accretion due to the inflowing nature of the BLR, and then once that accretion surpassed the Eddington limit the radiation pressure drives winds throughout the BLR producing an outflowing kinematic signature.

In the cases of NGC 5548 (M. Xiao et al. 2018) and NGC 4151 (Y.-J. Chen et al. 2023), they measured how the radius of the BLR ($R_{\rm BLR}$) changed as a function of continuum luminosity by cross correlating the continuum light curve and the measured BLR radius as function of time. In both cases, they found that the BLR radius changed on the timescales of ∼years, suggesting that BLR kinematics are a combined effect of radiation pressure and virialized gas that is bound to the BH.

We test the idea of alternative mechanisms driving the BLR kinematics by investigating if there is an offset between the measured BLR radii and the continuum luminosity. We have measured the BLR radius via integrated reverberation mapping in six different seasons (or years): 2014, 2016, 2017, 2021, 2022, and 2023 (the best-fit `PyROA` light curves for these years are shown in Appendix B). The BLR is assumed to respond to the central continuum on recombination timescales (J. H. Krolik et al. 1991; E. M. Cackett et al. 2007). We compare the aforementioned measured radii to the expectation of the recombination timescale in Figure 10.

If the lags and the recombination expectation line up closely, then the system is consistent with what we expect from photoionization physics. Namely, photoionization-driven optimal emitting regions of the BLR with a short recombination timescale. A scenario where the BLR is flowing in and out due to radiative winds would instead have an "adjustment delay," of the order of the dynamical time, between the expectation value and the corresponding BLR radius.

---

[28] https://www.asc.ohio-state.edu/astronomy/agnwatch/

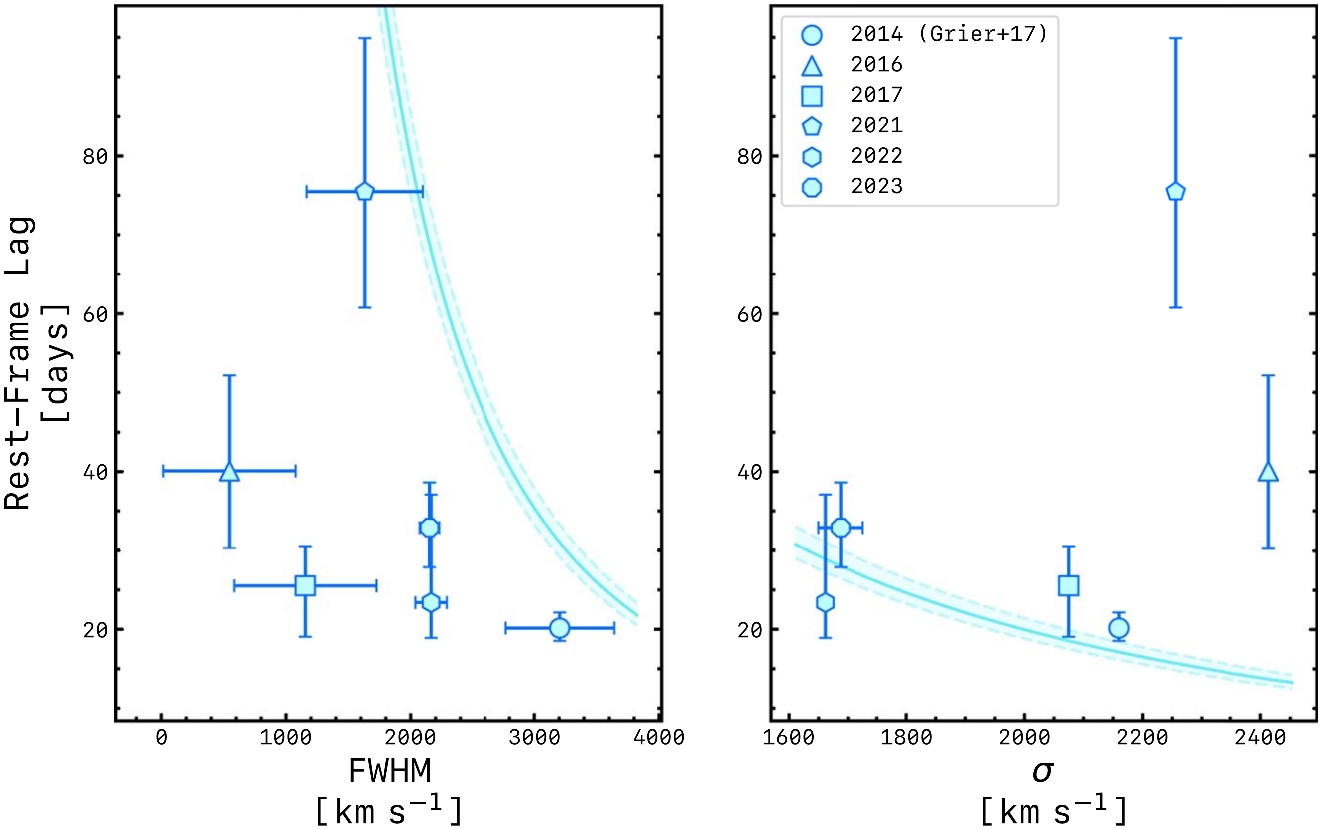

Figure 11. Rest-frame lag vs. line width (FWHM and σ) for Hβ in RM160. The left panel shows the rest-frame lag vs. FWHM and the right panel shows the rest-frame lag vs. σ. Different marker shapes indicate different monitoring periods as indicated by the legend. In both panels, the solid blue line indicates the line of constant Hβ-derived mass (indicating the virial product) from C. J. Grier et al. (2017) with the shaded blue region being the errors in the Hβ mass. We see that the measurements of FWHM and σ for Hβ do not follow the line of constant mass and therefore the virial product is not constant. This indicates that the virial product is not constant, indicating nonvirial and variable BLR kinematics such that the estimated BH mass could plausibly be incorrect.

We find that our measured BLR does not significantly differ from a recombination timescale expectation of BLR variations and we do not see an "adjustment time" to the measured BLR radii, in contrast to the systems studied by M. Xiao et al. (2018) and Y.-J. Chen et al. (2023).

5.4. Implications for Black Hole Mass in High-redshift Quasars

The foundation of black hole mass estimation beyond the local Universe rests on the assumption that the BLR is moving in orbits dominated by gravity (i.e., virial motion). This is true both for masses from reverberation mapping, and for the single-epoch masses based on the radius–luminosity relation (M. C. Bentz et al. 2013) that is calibrated by reverberation mapping. black hole mass estimates via reverberation mapping are found using

$$M = f\frac{v^2 R_{\rm BLR}}{G}, \tag{2}$$

where v is the width of a particular broad emission line, $R_{\rm BLR}$ is the optimal emission radius of that line using $R_{\rm BLR} = c\tau$, G is the gravitational constant, and f is a dimensionless factor that is introduced to compensate for our ignorance of the BLR kinematics, geometry, and orientation.

The VRLPs from RM160 indicate that the Hβ low and high states are inflowing as well as the Hα high state. This presence of nonvirial kinematics within the BLR of RM160 puts pressure on the foundation of black hole mass estimation. Moreover, even further pressure is put on the foundation of black hole mass estimation by the observation that we see the inferred Hα kinematics change from one state to the next in RM160.

In order to understand if the changing kinematics of BLR affects the mass measurement of RM160, we test the stability of the virial product. In Equation (2), the virial product is the $v^2 R_{\rm BLR}/G$ term. This term should be constant such that v^2 and $R_{\rm BLR}$ essentially compensate for each other (i.e., if $R_{\rm BLR}$ increases, v^2 decreases). In Figures 11 and 12, we plot the virial product (for both FWHM and σ measured from the rms spectrum) for six different time periods (the best-fit `PyROA` light curves for these years are shown in Appendix B). In both Figures 11 and 12, the solid line indicates the line of constant mass from C. J. Grier et al. (2017; i.e., points lying on this line would have a constant virial product) and the shaded region represents the errors in the mass. We see that for both Hβ and Hα, both the FWHM and σ do not follow this line of constant mass and therefore the virial product is not constant in RM160. The BLR radius and velocity (from both FWHM and σ) do not obey a constant virial product.

Figures 11 and 12 demonstrate that the virial product of RM160 is not constant over the entire monitoring period of 2013–2023. The variable BLR kinematics suggests that the basic assumption behind BH mass, a virial BLR bound to the central black hole, is fundamentally flawed. As mentioned in L. B. Fries et al. (2023), RM160 was chosen for its unusual

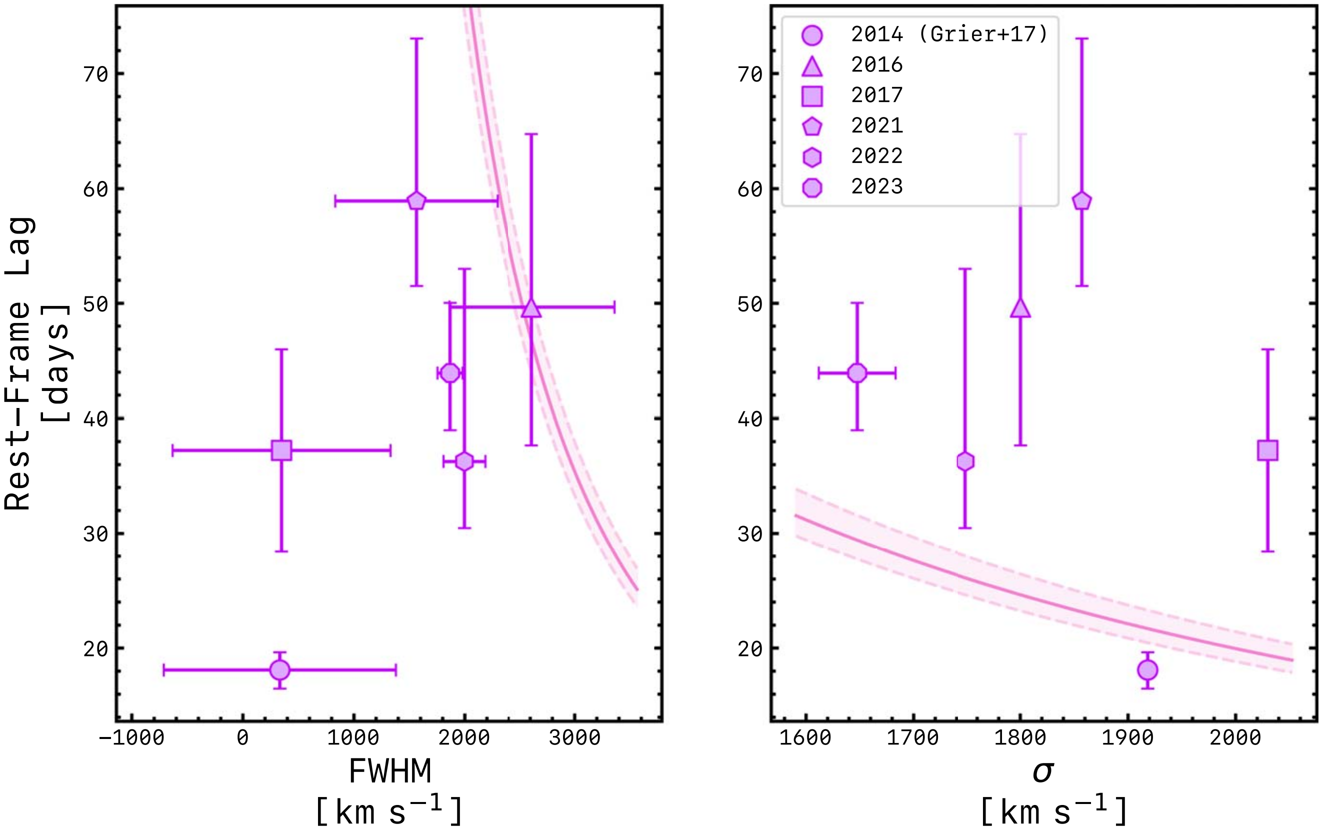

Figure 12. Rest-frame lag vs. line width (FWHM and σ) for Hα in RM160. The left panel shows the rest-frame lag vs. FWHM and the right panel shows the rest-frame lag vs. σ. Different marker shapes indicate different monitoring periods as indicated by the legend. In both panels, the solid purple line indicates the line of constant Hα-derived mass (indicating the virial product) from C. J. Grier et al. (2017) with the shaded purple region being the errors in the Hα mass. We see that the measurements of FWHM and σ for Hα do not follow the line of constant mass and therefore the virial product is not constant. This indicates that in the presence of nonvirial and changing BLR kinematics, the virial product fails to be constant and the estimated BH mass could plausibly be incorrect.

line-profile variability, but these observations do not exist for most AGN (and despite the difficulties of SNR, cadence, and duration, there are two similar AGN reported in the literature; M. Xiao et al. 2018; Y.-J. Chen et al. 2023). It is possible that luminous quasars, probed by SDSS-RM and BHM-RM but unexplored by previous decades of single-object RM studies, are more likely to have nonvirial BLR kinematics due to larger radiation pressure. More studies of luminous quasars with velocity-resolved RM are needed to understand if the basic assumptions of BH masses are valid for all AGN.

6. Conclusions

We have presented velocity-resolved reverberation mapping of the luminous quasar RM160. We split the light curves into two states corresponding with the 3× increase in flux: the low state from 2013 to 2019 and the high state from 2022 to 2023. We find that the inferred kinematics from the velocity-resolved analysis is different between the Balmer lines and, more so for Hα, they change from low state to high state. We find that changes in the BLR radii correspond to the continuum luminosity variations of the quasar, consistent with a short recombination timescale and not requiring a longer dynamical adjustment time associated with restructuring of the BLR gas. We also find that the virial product throughout the monitoring period is nonconstant, offering many questions for the enterprise of black hole mass measurements.

We interpret the differences between the Balmer lines as a product of radial stratification in the BLR where, due to optical depth effects, the Hα-responding region is further out from the Hβ-responding region. This implies that the BLR kinematics in RM160 is stratified as well such that the kinematics is not ubiquitous throughout the BLR.

We interpret the inferred kinematic evolution of Hα as kinematic stratification in the BLR, whereby the part of the BLR probed by the Hα low state is further from the black hole and virial. Conversely, in the high state the Hα part of the BLR being probed is closer in and inflowing, which agrees with the Hβ radii and kinematics for both states.

We examine the time delay between changes in the BLR radii and luminosity and find that the time delay is of the same magnitude as the recombination timescale unlike some recent velocity-resolved reverberation mapping studies (M. Xiao et al. 2018; Y.-J. Chen et al. 2023). This effectively tests, and verifies, the assumption of BLR variation on the recombination timescales for this object.

Finally, we examine the stability of the virial product in RM160. We find that the virial product, in both FWHM and σ, for the Balmer lines is not constant (i.e., they do not follow the line of constant mass). This is plausibly due to the nonvirial and changing kinematics inferred from our velocity-resolved reverberation mapping analysis. The nonvirial nature of a luminous quasar like RM160 could have broad implications for BH mass estimates in high-redshift quasars. If there is a significant nonvirial contribution to the BLRs kinematics, then the masses will be dramatically overestimated due to the added velocity from nonvirial kinematics.

Since this study only examines a single object, we do not have a good sense for how rare (or common) the inconsistent virial product phenomenon is. Most studies investigating BLR kinematics have used low-redshift Seyfert 1 AGN (M. C. Bentz et al. 2009; A. J. Barth et al. 2011; P. Du et al. 2016; V. U et al. 2022), but our understanding of black hole growth over cosmic time relies heavily on our knowledge of luminous quasars. This study does represent a caution for the interpretation of black hole masses for individual luminous quasars unless the stability of the virial product can be shown through time-domain spectroscopy. Unfortunately, this is challenging for high-redshift quasars because of cosmological time dilation.

Instead, we might rely on the line profile. In the case of RM160, the broad emission lines are significantly redshifted compared to the systemic narrow lines and the broad emission-line profiles are significantly boxier than Gaussian (L. B. Fries et al. 2023). The shape of the broad emission-line profile was also identified by L. Villafaña et al. (2022) as a possible contributor to spectroscopic mass measurement values. Considering recent JWST observations of overmassive black holes in the early Universe (Y. Harikane et al. 2023; R. Maiolino et al. 2023; F. Pacucci et al. 2023), we suggest caution in black hole mass estimates in high-redshift quasars as nonvirial kinematics could be dramatically overestimating the masses of these black holes. More studies of velocity-resolved lags in luminous QSOs are needed to determine if the variable kinematics of RM160 are common or unusual.

Acknowledgments

L.B.F., J.R.T., and M.C.D. acknowledge support from NSF grant CAREER-1945546, and with C.J.G. acknowledges support from NSF grant AST-2108668. J.R.T., C.J.G., and Y.S. also acknowledge support from NSF grants AST-2009539 and AST-2009947. M.K. acknowledges support by DFG grant No. KR 3338/4-1. B.T. acknowledges support from the European Research Council (ERC) under the European Union’s Horizon 2020 research and innovation program (grant agreement 950533) and from the Israel Science Foundation (grant No. 1849/19). X.L. acknowledges support from NSF grant AST-2206499. C.R. acknowledges support from the Fondecyt Iniciación grant No. 11190831 and ANID BASAL project FB210003. R.J.A. was supported by FONDECYT grant No. 1231718 and by the ANID BASAL project FB210003. M.L.M.-A. acknowledges financial support from Millenium Nucleus NCN19_058 (TITANs). P.B.H. acknowledges support from NSERC grant No. 2023-05068.

Funding for the Sloan Digital Sky Survey V has been provided by the Alfred P. Sloan Foundation, the Heising-Simons Foundation, the National Science Foundation, and the Participating Institutions. SDSS acknowledges support and resources from the Center for High-Performance Computing at the University of Utah. SDSS telescopes are located at Apache Point Observatory, funded by the Astrophysical Research Consortium and operated by New Mexico State University, and at Las Campanas Observatory, operated by the Carnegie Institution for Science. The SDSS website is www.sdss.org.

SDSS is managed by the Astrophysical Research Consortium for the Participating Institutions of the SDSS Collaboration, including Caltech, The Carnegie Institution for Science, Chilean National Time Allocation Committee (CNTAC) ratified researchers, The Flatiron Institute, the Gotham Participation Group, Harvard University, Heidelberg University, The Johns Hopkins University, L’Ecole polytechnique fédérale de Lausanne (EPFL), Leibniz-Institut für Astrophysik Potsdam (AIP), Max-Planck-Institut für Astronomie (MPIA Heidelberg), Max-Planck-Institut für Extraterrestrische Physik (MPE), Nanjing University, National Astronomical Observatories of China (NAOC), New Mexico State University, The Ohio State University, Pennsylvania State University, Smithsonian Astrophysical Observatory, Space Telescope Science Institute (STScI), the Stellar Astrophysics Participation Group, Universidad Nacional Autónoma de México, University of Arizona, University of Colorado Boulder, University of Illinois at Urbana-Champaign, University of Toronto, University of Utah, University of Virginia, Yale University, and Yunnan University.

L.B.F. is deeply indebted to Bren Backhaus and Jonathan Mercedes Feliz for their invaluable scientific and data visualization discussions.

Software: `AstroPy` (Astropy Collaboration et al. 2013, 2018), `Matplotlib` (J. D. Hunter 2007), `NumPy` (C. R. Harris et al. 2020), `SciPy` (P. Virtanen et al. 2020), and `PyROA` (F. R. Donnan et al. 2021).

Appendix A
Velocity-resolved `PyROA` Fits

We present our velocity-resolved `PyROA` best-fit models here in Figures 13–16 that are discussed in Section 4.1.

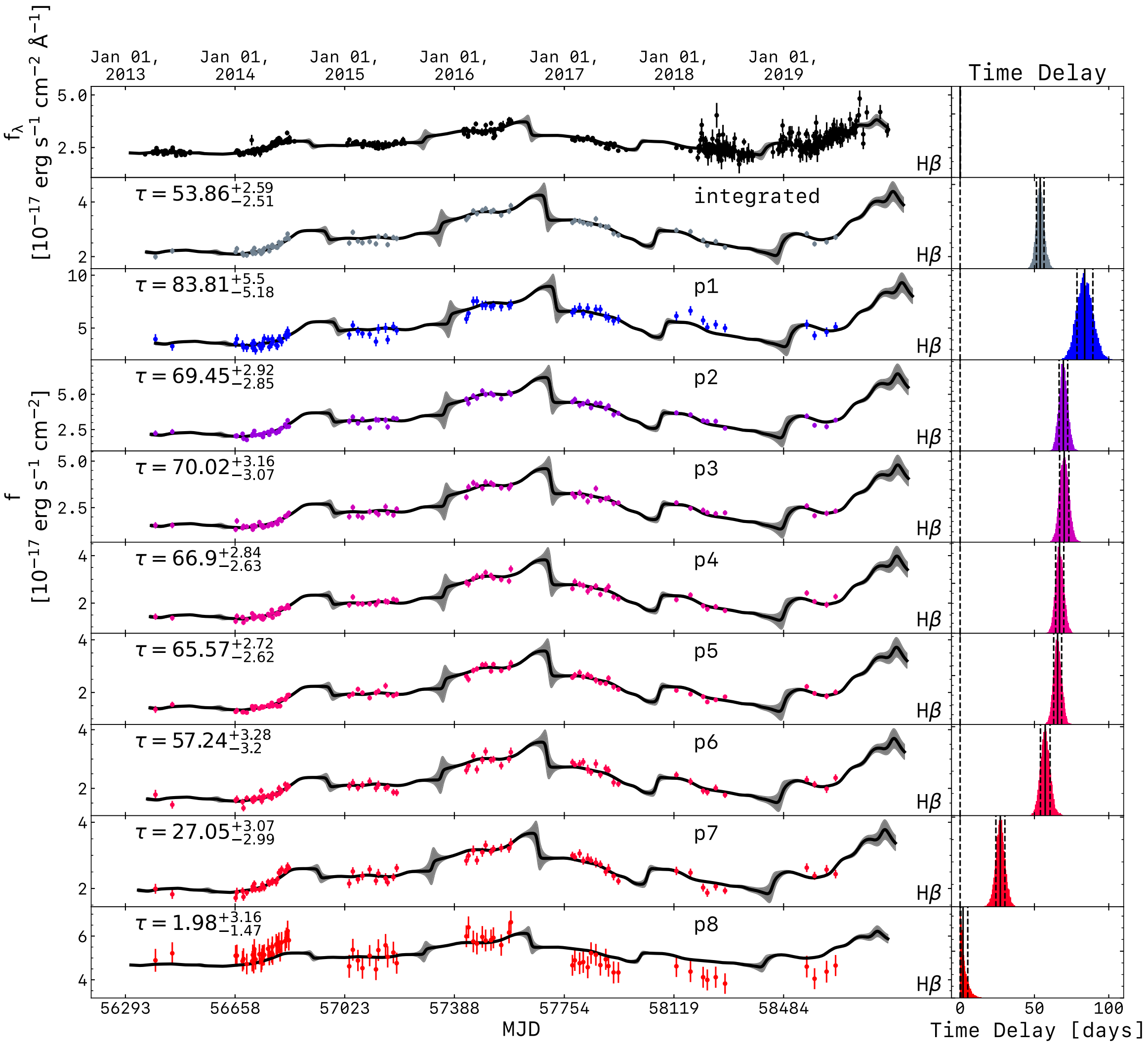

Figure 13. Low-state Hβ velocity-resolved light curves with the best-fit `PyROA` model overlaid as a solid black line with the corresponding error envelope. The top panel shows the continuum light curve, the panel below that shows the integrated light curve, and subsequent light curves are the partitioned light curves (colored from blue to red). Each partitioned light curve is labeled "p#," where # is the partition number outlined in Table 2. The best-fit time delays along with their corresponding errors are shown in the top left of each light curve. The posterior distribution for the time delay is on the right panel of each responding light curve where the median value and 68th percentile errors are the solid and dashed lines, respectively.

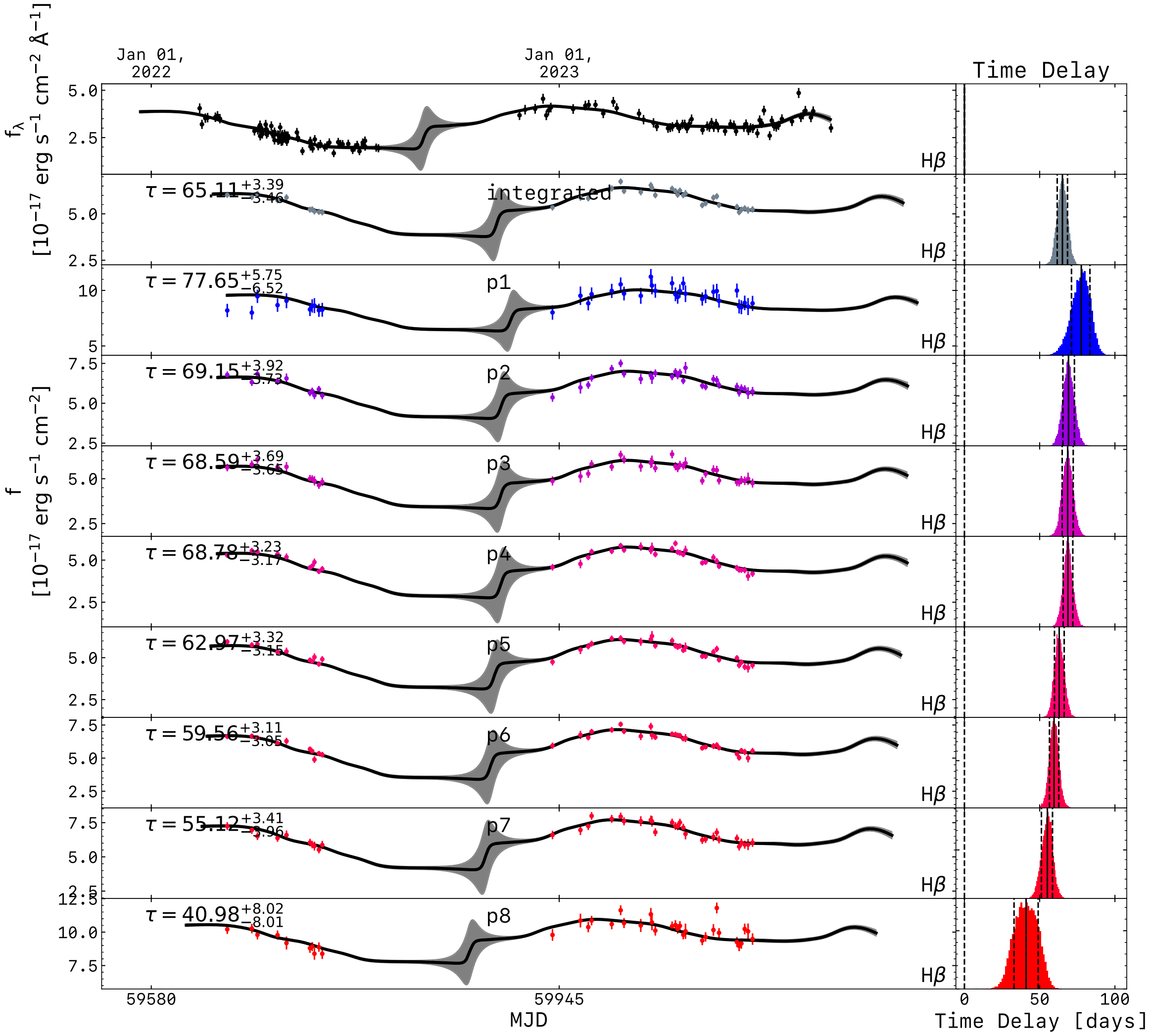

Figure 14. High-state Hβ velocity-resolved light curves with the best-fit `PyROA` model overlaid as a solid black line with the corresponding error envelope. The top panel shows the continuum light curve, the panel below that shows the integrated light curve, and subsequent light curves are the partitioned light curves (colored from blue to red). Each partitioned light curve is labeled "p#," where # is the partition number outlined in Table 2. The best-fit time delays along with their corresponding errors are shown in the top left of each light curve. The posterior distribution for the time delay is on the right panel of each responding light curve where the median value and 68th percentile errors are the solid and dashed lines, respectively.

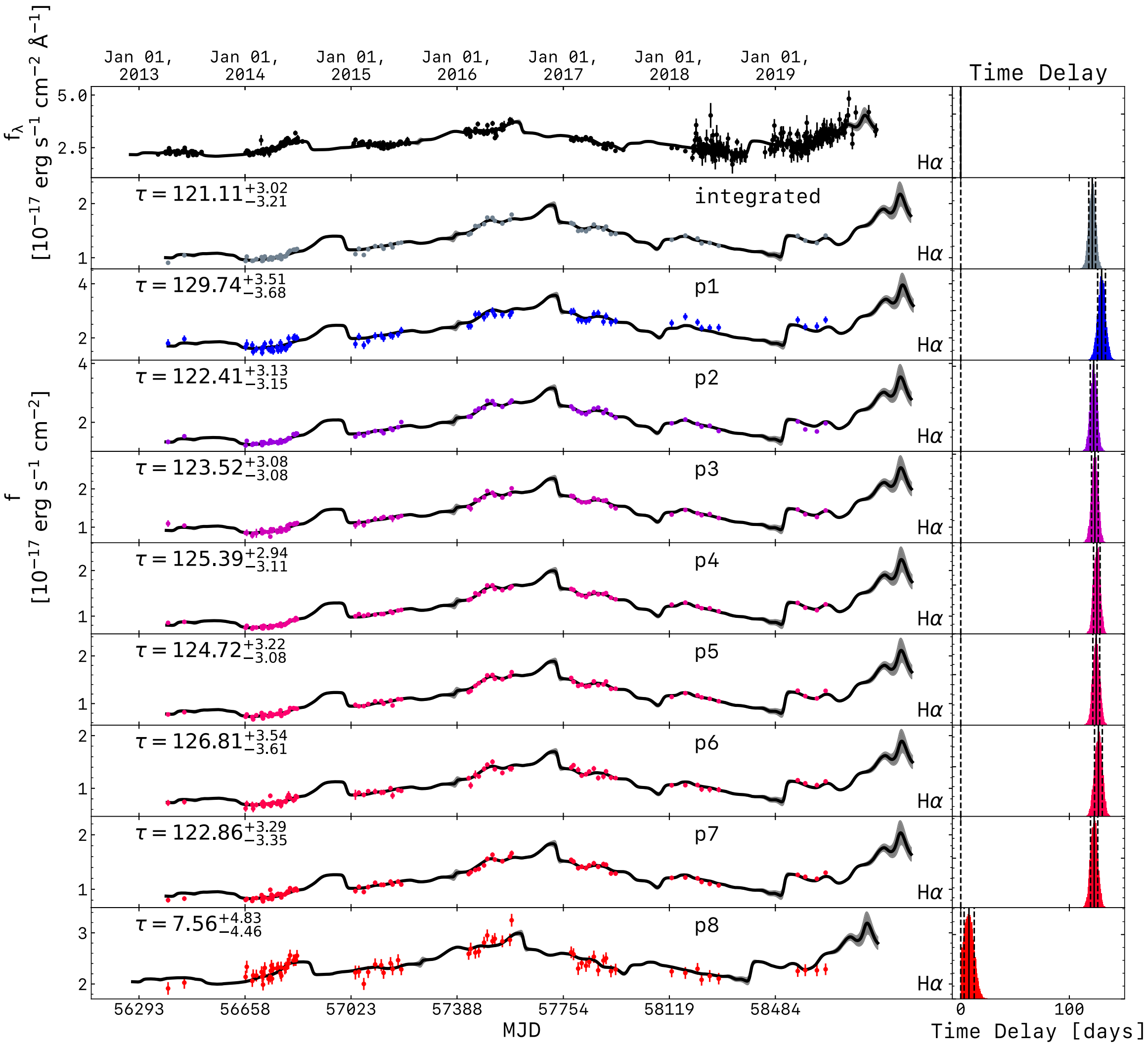

Figure 15. Low-state Hα velocity-resolved light curves with the best-fit `PyROA` model overlaid as a solid black line with the corresponding error envelope. The top panel shows the continuum light curve, the panel below that shows the integrated light curve, and subsequent light curves are the partitioned light curves (colored from blue to red). Each partitioned light curve is labeled "p#," where # is the partition number outlined in Table 2. The best-fit time delays along with their corresponding errors are shown in the top left of each light curve. The posterior distribution for the time delay is on the right panel of each responding light curve where the median value and 68th percentile errors are the solid and dashed lines, respectively.

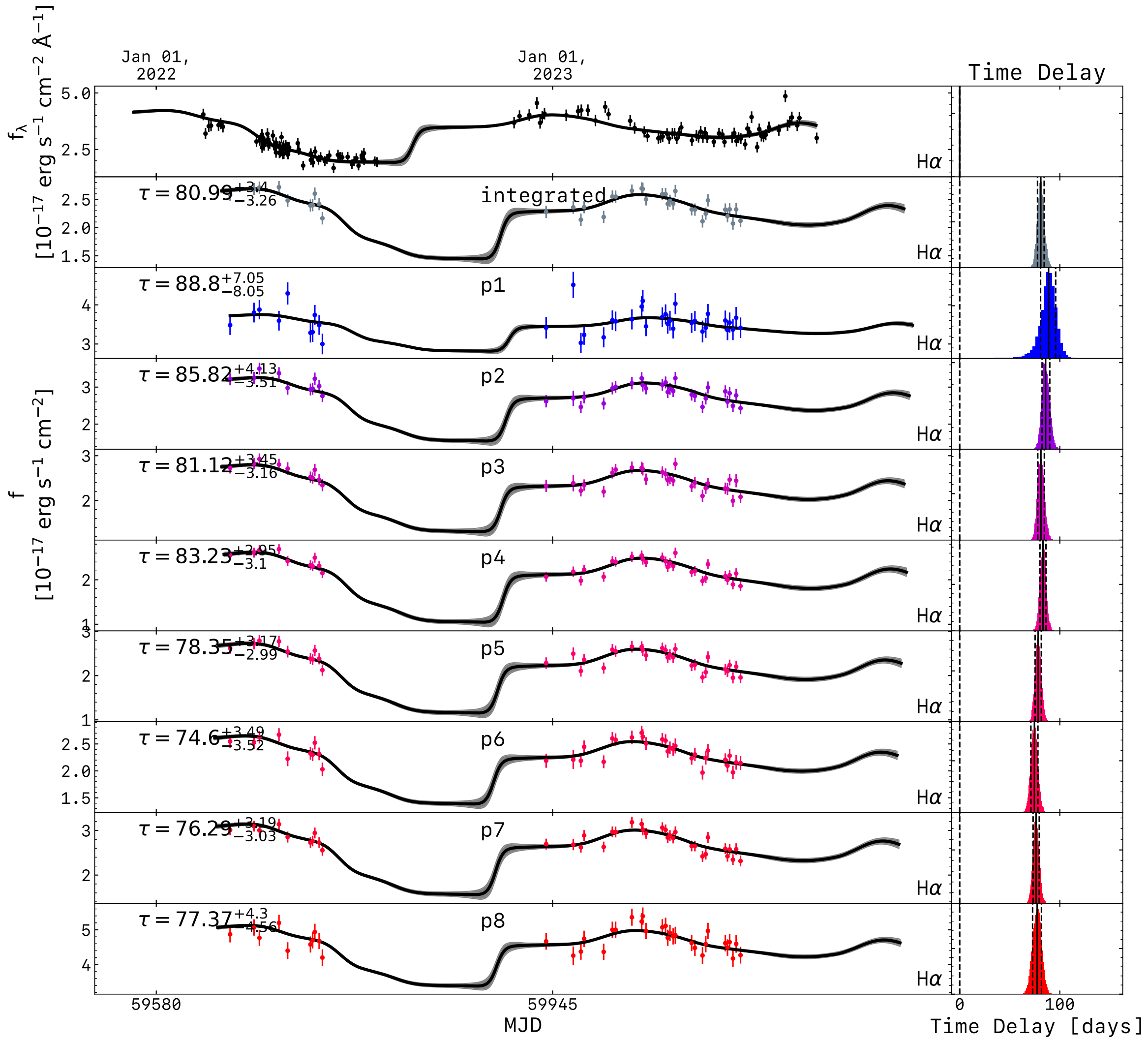

Figure 16. High-state Hα velocity-resolved light curves with the best-fit `PyROA` model overlaid as a solid black line with the corresponding error envelope. The top panel shows the continuum light curve, the panel below that shows the integrated light curve, and subsequent light curves are the partitioned light curves (colored from blue to red). Each partitioned light curve is labeled "p#," where # is the partition number outlined in Table 2. The best-fit time delays along with their corresponding errors are shown in the top left of each light curve. The posterior distribution for the time delay is on the right panel of each responding light curve where the median value and 68th percentile errors are the solid and dashed lines, respectively.

Appendix B
Virial Product Seasonal `PyROA` Fits

We present our seasonal integrated lag measurements for the years 2014, 2016, 2017, 2021, 2022, and 2023 in Figure 17. These lags are the measurements shown in Figures 10–12.

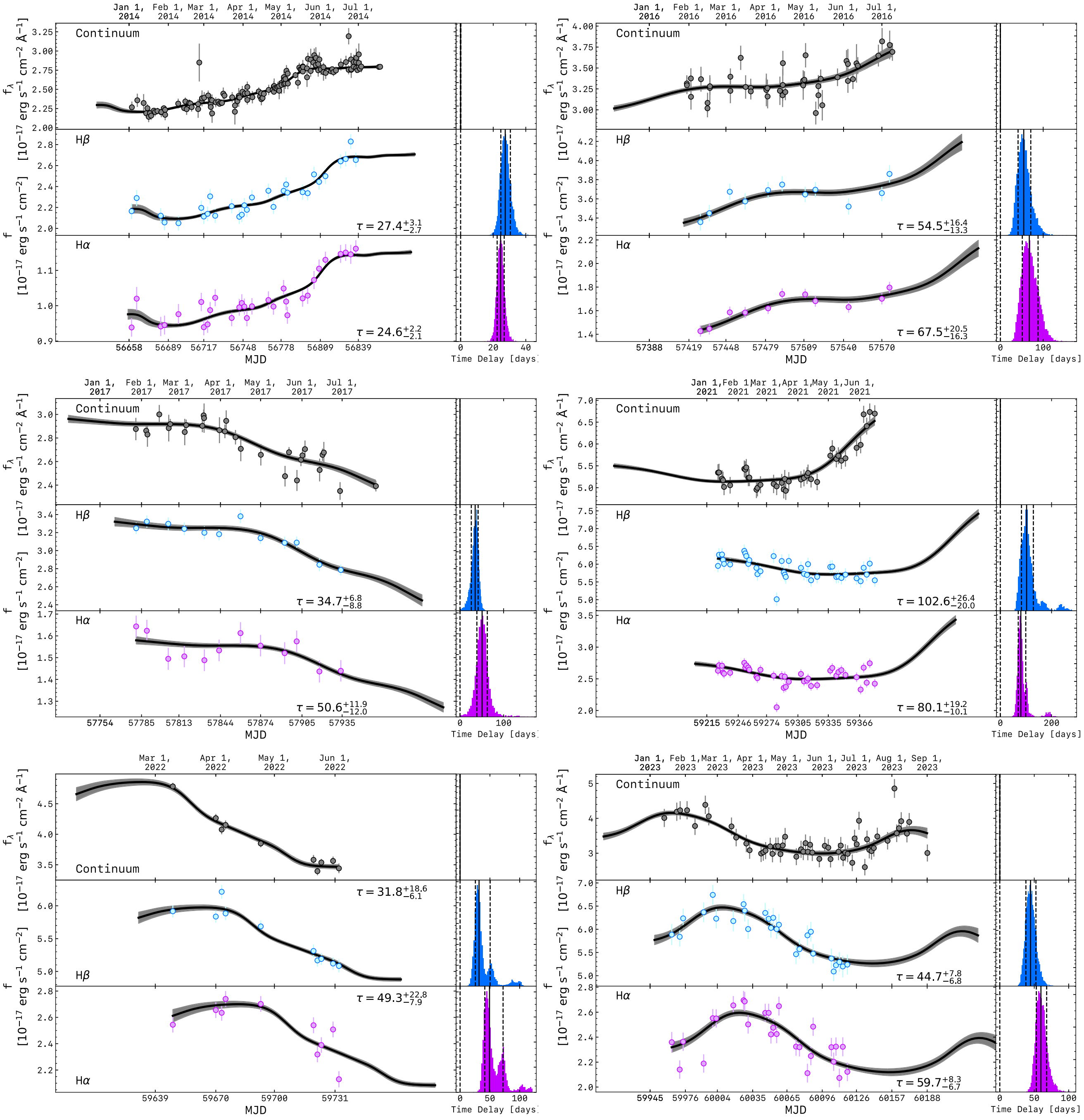

Figure 17. Best-fit `PyROA` light curves for the seasons shown in Figures 10–12. Years 2014 and 2016, 2017 and 2021, and 2022 and 2023 are shown from left to right in the top, middle, and bottom panels, respectively.

ORCID iDs

Logan B. Fries https://orcid.org/0000-0001-8032-2971
Jonathan R. Trump https://orcid.org/0000-0002-1410-0470
Keith Horne https://orcid.org/0000-0003-1728-0304
Megan C. Davis https://orcid.org/0000-0001-9776-9227
Catherine J. Grier https://orcid.org/0000-0001-9920-6057
Yue Shen https://orcid.org/0000-0003-1659-7035
Scott F. Anderson https://orcid.org/0000-0002-6404-9562
Tom Dwelly https://orcid.org/0000-0002-4459-9233
Y. Homayouni https://orcid.org/0000-0002-0957-7151
Sean Morrison https://orcid.org/0000-0002-6770-2627
Jessie C. Runnoe https://orcid.org/0000-0001-8557-2822
Benny Trakhtenbrot https://orcid.org/0000-0002-3683-7297
Roberto J. Assef https://orcid.org/0000-0002-9508-3667
Dmitry Bizyaev https://orcid.org/0000-0002-3601-133X
W. N. Brandt https://orcid.org/0000-0002-0167-2453
Peter Breiding https://orcid.org/0000-0003-1317-8847
Joel Brownstein https://orcid.org/0000-0002-8725-1069
Priyanka Chakraborty https://orcid.org/0000-0002-4469-2518
P. B. Hall https://orcid.org/0000-0002-1763-5825
Anton M. Koekemoer https://orcid.org/0000-0002-6610-2048
Héctor J. Ibarra-Medel https://orcid.org/0000-0002-9790-6313
Mary Loli Martínez-Aldama https://orcid.org/0000-0002-7843-7689
C. Alenka Negrete https://orcid.org/0000-0002-1656-827X
Kaike Pan https://orcid.org/0000-0002-2835-2556
Claudio Ricci https://orcid.org/0000-0001-5231-2645
Donald P. Schneider https://orcid.org/0000-0001-7240-7449
Hugh W. Sharp https://orcid.org/0000-0001-9616-1789
Theodore B. Smith https://orcid.org/0009-0003-8591-0061
Zachary Stone https://orcid.org/0000-0002-8501-3518
Matthew J. Temple https://orcid.org/0000-0001-8433-550X

References

Astropy Collaboration, Price-Whelan, A. M., Sipőcz, B. M., et al. 2018, AJ, 156, 123
Astropy Collaboration, Robitaille, T. P., Tollerud, E. J., et al. 2013, A&A, 558, A33
Barth, A. J., Bennert, V. N., Canalizo, G., et al. 2015, ApJS, 217, 26
Barth, A. J., Pancoast, A., Thorman, S. J., et al. 2011, ApJL, 743, L4
Baskin, A., & Laor, A. 2018, MNRAS, 474, 1970
Bentz, M. C., Denney, K. D., Grier, C. J., et al. 2013, ApJ, 767, 149
Bentz, M. C., Horne, K., Barth, A. J., et al. 2010a, ApJL, 720, L46
Bentz, M. C., Walsh, J. L., Barth, A. J., et al. 2009, ApJ, 705, 199
Bentz, M. C., Walsh, J. L., Barth, A. J., et al. 2010b, ApJ, 716, 993
Bentz, M. C., Williams, P. R., Street, R., et al. 2021, ApJ, 920, 112
Bischoff, K., & Kollatschny, W. 1999, A&A, 345, 49
Blandford, R. D., & McKee, C. F. 1982, ApJ, 255, 419
Blanton, M. R., Bershady, M. A., Abolfathi, B., et al. 2017, AJ, 154, 28
Bolton, A. S., Schlegel, D. J., Aubourg, É., et al. 2012, AJ, 144, 144
Cackett, E. M., Bentz, M. C., & Kara, E. 2021, iSci, 24, 102557
Cackett, E. M., Gelbord, J., Barth, A. J., et al. 2023, ApJ, 958, 195
Cackett, E. M., Horne, K., & Winkler, H. 2007, MNRAS, 380, 669
Chen, Y.-J., Bao, D.-W., Zhai, S., et al. 2023, MNRAS, 520, 1807
De Rosa, G., Fausnaugh, M. M., Grier, C. J., et al. 2018, ApJ, 866, 133
De Rosa, G., Peterson, B. M., Ely, J., et al. 2015, ApJ, 806, 128
Denney, K. D., Peterson, B. M., Pogge, R. W., et al. 2009a, ApJL, 704, L80
Denney, K. D., Watson, L. C., Peterson, B. M., et al. 2009b, ApJ, 702, 1353
Donnan, F. R., Hernández Santisteban, J. V., Horne, K., et al. 2023, MNRAS, 523, 545
Donnan, F. R., Horne, K., & Hernández Santisteban, J. V. 2021, MNRAS, 508, 5449
Du, P., Lu, K.-X., Hu, C., et al. 2016, ApJ, 820, 27
Eisenstein, D. J., Weinberg, D. H., Agol, E., et al. 2011, AJ, 142, 72
Flewelling, H. A., Magnier, E. A., Chambers, K. C., et al. 2020, ApJS, 251, 7
Fries, L. B., Trump, J. R., Davis, M. C., et al. 2023, ApJ, 948, 5
Gaskell, C. M., & Sparke, L. S. 1986, ApJ, 305, 175
Gravity Collaboration, Amorim, A., Bauböck, M., et al. 2020, A&A, 643, A154
Grier, C. J., Peterson, B. M., Horne, K., et al. 2013, ApJ, 764, 47
Grier, C. J., Trump, J. R., Shen, Y., et al. 2017, ApJ, 851, 21
Gunn, J. E., Siegmund, W. A., Mannery, E. J., et al. 2006, AJ, 131, 2332
Guo, H., Shen, Y., He, Z., et al. 2020, ApJ, 888, 58
Harikane, Y., Zhang, Y., Nakajima, K., et al. 2023, ApJ, 959, 39
Harris, C. R., Millman, K. J., van der Walt, S. J., et al. 2020, Natur, 585, 357
Homayouni, Y., Trump, J. R., Grier, C. J., et al. 2020, ApJ, 901, 55
Horne, K. 1994, in ASP Conf. Ser. 69, Reverberation Mapping of the Broad-Line Region in Active Galactic Nuclei, ed. P. M. Gondhalekar, K. Horne, & B. M. Peterson (San Francisco, CA: ASP), 23
Horne, K., De Rosa, G., Peterson, B. M., et al. 2021, ApJ, 907, 76
Horne, K., Peterson, B. M., Collier, S. J., & Netzer, H. 2004, PASP, 116, 465
Hunter, J. D. 2007, CSE, 9, 90
Kinemuchi, K., Hall, P. B., McGreer, I., et al. 2020, ApJS, 250, 10
Kollatschny, W., Ochmann, M. W., Zetzl, M., et al. 2018, A&A, 619, A168
Kollmeier, J., Anderson, S. F., Blanc, G. A., et al. 2019, BAAS, 51, 274
Korista, K. T., & Goad, M. R. 2004, ApJ, 606, 749
Krolik, J. H., Horne, K., Kallman, T. R., et al. 1991, ApJ, 371, 541
Li, S.-S., Feng, H.-C., Liu, H. T., et al. 2022, ApJ, 936, 75
Li, Y.-R., Songsheng, Y.-Y., Qiu, J., et al. 2018, ApJ, 869, 137
Li, Y.-R., Wang, J.-M., Ho, L. C., Du, P., & Bai, J.-M. 2013, ApJ, 779, 110
Li, Y.-R., Wang, J.-M., Hu, C., Du, P., & Bai, J.-M. 2014, ApJL, 786, L6
Lu, K.-X., Bai, J.-M., Wang, J.-M., et al. 2022, ApJS, 263, 10
Maiolino, R., Scholtz, J., Curtis-Lake, E., et al. 2023, arXiv:2308.01230
Masci, F. J., Laher, R. R., Rusholme, B., et al. 2019, PASP, 131, 018003
Netzer, H. 1975, MNRAS, 171, 395
Pacucci, F., Nguyen, B., Carniani, S., Maiolino, R., & Fan, X. 2023, ApJL, 957, L3
Pancoast, A., Brewer, B. J., & Treu, T. 2011, ApJ, 730, 139
Pancoast, A., Brewer, B. J., Treu, T., et al. 2014, MNRAS, 445, 3073
Pei, L., Fausnaugh, M. M., Barth, A. J., et al. 2017, ApJ, 837, 131
Peterson, B. M. 1993, PASP, 105, 247
Peterson, B. M., Ferrarese, L., Gilbert, K. M., et al. 2004, ApJ, 613, 682
Rees, M. J., Netzer, H., & Ferland, G. J. 1989, ApJ, 347, 640
Sayres, C., Sánchez-Gallego, J. R., Blanton, M. R., et al. 2022, Proc. SPIE, 12184, 121847K
Seyfert, C. K. 1943, ApJ, 97, 28
Shen, Y., Brandt, W. N., Dawson, K. S., et al. 2015, ApJS, 216, 4
Shen, Y., Grier, C. J., Horne, K., et al. 2024, ApJS, 272, 26
Shen, Y., Hall, P. B., Horne, K., et al. 2019, ApJS, 241, 34
Smee, S. A., Gunn, J. E., Uomoto, A., et al. 2013, AJ, 146, 32
U, V., Barth, A. J., Vogler, H. A., et al. 2022, ApJ, 925, 52
Villafaña, L., Williams, P. R., Treu, T., et al. 2022, ApJ, 930, 52
Virtanen, P., Gommers, R., Oliphant, T. E., et al. 2020, NatMe, 17, 261
Wang, S., Shen, Y., Jiang, L., et al. 2020, ApJ, 903, 51
Xiao, M., Du, P., Lu, K.-K., et al. 2018, ApJL, 865, L8
York, D. G., Adelman, J., Anderson, J. E. J., et al. 2000, AJ, 120, 1579